Large-eddy simulation of a very large wind farm in a stable atmospheric boundary layer

Hao Lu,[1,*] Fernando Porté-Agel[1,2,†]
[1]Saint Anthony Falls Laboratory, Civil Engineering, University of Minnesota - Twin Cities, 2 Third Ave SE, Minneapolis, MN 55414, USA
[2]School of Architecture, Civil and Environmental Engineering (ENAC), École Polytechnique Fédérale de Lausanne (EPFL), CH-1015 Lausanne, Switzerland

June 16, 2011

Abstract

When deployed as large arrays, wind turbines significantly interact among themselves and with the atmospheric boundary layer. In this study, we integrate a three-dimensional large-eddy simulation with an actuator line technique to examine the characteristics of wind-turbine wakes in an idealized wind farm inside a redstable boundary layer (SBL). The wind turbines, with a rotor diameter of 112 m and a tower height of 119 m, were "immersed" in a well-known SBL case that bears a boundary layer height of approximately 175 m. Two typical spacing setups were adopted in this investigation. The super-geostrophic low-level jet near the top of the boundary layer was eliminated owing to the energy extraction and the enhanced mixing of momentum. Non-axisymmetric wind-turbine wakes were observed in response to the non-uniform incoming turbulence, the Coriolis effect, and the rotational effects induced by blade motion. The Coriolis force caused a skewed spatial structure and drove a part of the turbulence energy away from the center of the wake. The SBL height was increased, while the magnitude of the surface momentum flux was reduced by more than 30%, and the magnitude of the surface buoyancy flux was reduced by more than 15%. The wind farm was also found to have a strong effect on vertical turbulent fluxes of momentum and heat, an outcome that highlights the potential impact of wind farms on local meteorology.

1 Introduction

The atmospheric boundary layer (ABL), known as the most important atmospheric component for wind-power applications, is a high-Reynolds-number turbulent boundary layer flow ($Re \sim O(10^9)$) whose structure and dynamics are strongly modulated by the variability of land-surface forcings (e.g., the diurnal cycle of surface temperature). With the fast growth of the wind-energy sector worldwide, the interaction between ABL flow and wind turbines, and the cumulative effects of turbine wakes, have become important issues in both the wind energy and the atmospheric science

*E-mail: hao.lu@live.com
†E-mail: fernando.porte-agel@epfl.ch

communities [1, 2, 3, 4, 5, 6]. Accurate prediction of ABL flow and of its interactions with wind turbines is critical for optimizing the siting of wind turbines and the layout of wind farms. In particular, flow prediction can be used to maximize wind-energy production and minimize fatigue loads in wind farms. Numerical simulations can also provide valuable quantitative insight into the potential impacts of wind farms on local meteorology. These are associated with the significant role of wind turbines in slowing down the wind and enhancing vertical mixing of momentum, heat, moisture, and other scalars.

Of special interest for wind-energy applications is the study of the redstable boundary layer (SBL), which typically develops during the night in mid-latitudes, and also during the day in cold regions (e.g., polar regions). Under these conditions, the surface is colder than the surrounding air, the flow stratifies and turbulence is generated by shear and destroyed by dissipation and negative buoyancy. SBLs are relatively shallow and are characterized by strong vertical shear and a relatively high wind near the top of the boundary layer. At that height, the wind can become super-geostrophic and form the so-called low-level jet. Moreover, the Coriolis effect associated with planetary rotation leads to a change of wind direction with height. This creates an additional lateral shear, which is considerable for large-sized wind turbines. As a result, compared with daytime boundary layers, SBLs provide not only larger energy potential, but also larger structural fatigue loads associated with strong vertical and lateral shear.

The turbulence parameterization constitutes the most critical part of turbulent-flow simulations. It was realized early that direct numerical simulations (DNSs) were not possible for most engineering and environmental turbulent flows, such as the ABL. Thus, the Reynolds-averaged Navier-Stokes (RANS) approach was adopted in most previous studies [7, 8, 9, 10, 11, 12, 13] on ABL flow through a single wind turbine or wind farm. However, as repeatedly reported in a variety of contexts [14, 15, 16], RANS computes the mean flow and models the effect of unsteady turbulent velocity fluctuations according to a variety of physical approximations. Consequently, it is too dependent on the characteristics of particular flows to be used as a method of general applicability. Large-eddy simulation (LES) was developed as an intermediate approximation between DNS and RANS, the general idea being that the large, non-universal scales of the flow are computed explicitly, while the small scales are modeled. Large-eddy simulation can potentially provide the kind of high-resolution spatial and temporal information needed to maximize wind-energy production and minimize fatigue loads in wind farms. The accuracy of LESs of ABL flow with wind turbines hinges on our ability to parameterize subgrid-scale (SGS) turbulent fluxes as well as turbine-induced forces. Only recently have there been some efforts [17, 18, 19] to apply LES to simulation redof wind-turbine wakes.

In LES of ABL flows, the SGS turbulent fluxes of momentum and heat are typically modeled using eddy-viscosity/diffusivity (Smagorinsky-type) models [20, 21]. One of the main challenges when applying these models is the specification of the model coefficients, which are known to depend on position in the flow, filter size, atmospheric stability, among other factors [22, 23]. A systematic way of computing the model coefficients is using the recently developed scale-dependent Lagrangian dynamic models, which optimize the local values of the SGS model coefficients and account for their scale dependence in a dynamic manner (using information of the resolved field and, thus, not requiring any tuning of parameters). In general, scale-dependent dynamic models [24, 25, 26, 27, 28] have been shown to represent the resolved flow statistics (e.g., mean velocity, turbulence intensity and energy spectra) near the surface better than the traditional Smagorinsky model or the standard (scale-invariant) dynamic models.

In industry nowadays, the only routinely used computational approach for wind-turbine aerodynamics is based on the blade-element momentum (BEM) theory. The concept was introduced by Froude [29] in 1889 as a continuation of the work of Rankine [30] on the momentum theory of propellers. A major step forward in wind-turbine modeling came with the development of the generalized momentum theory and the introduction of the BEM approach by Glauert [31]. The axial-symmetry assumption of wind-turbine modeling has been relaxed by a recently introduced actuator line method (ALM) [32], by which the loading is distributed along lines representing blade forces in a fully three-dimensional flow domain. The ALM includes the influence of the rotating blades on the flow field, and has the strength to capture important physics of the wind-turbine wake such as tip vortices and coherent periodic structures in helical wakes [32, 33, 34]. A drawback of the ALM is that it relies on airfoil characteristics that are not always available. However, some of the advantages attributable to the ALM include that it is easy to implement, it contains most of the physics representing rotary aerodynamics in wind-turbine wakes, and it has proven to be accurate for the most common flow conditions and rotor configurations.

This work is dedicated mainly to the study of SBL flow through an idealized large wind farm, with emphasis on the characteristics of wind-turbine wakes and their aggregated effect on land-atmosphere exchanges (momentum and heat fluxes). This is achieved by using an LES framework that integrates scale-dependent Lagrangian dynamic models for the SGS fluxes and the actuator line technique for the turbine-induced forces. This framework is described in section 2. Section 3 describes the case study and provides the simulation details. The LES results are presented and discussed in section 4, and a summary and conclusions are provided in section 5.

2 The large-eddy simulation framework

2.1 LES governing equations

The LES code used in this study is a modified version of the code used for previous studies [35, 24, 36, 25, 37, 38, 27, 39] of ABL flows. The code solves the filtered continuity equation, the filtered momentum conservation equations based on the Boussinesq approximation, and the filtered transport equation for potential temperature

$$\frac{\partial \widetilde{u}_i}{\partial x_i} = 0 \ , \tag{1}$$

$$\frac{\partial \widetilde{u}_i}{\partial t} + \widetilde{u}_j \frac{\partial \widetilde{u}_i}{\partial x_j} = -\frac{\partial \widetilde{p}^*}{\partial x_i} - \frac{\partial \tau_{ij}}{\partial x_j} + \delta_{i3} g \frac{\widetilde{\theta} - \left\langle \widetilde{\theta} \right\rangle}{\theta_0} + f_c \varepsilon_{ij3} \widetilde{u}_j + \mathcal{F}_i, \tag{2}$$

$$\frac{\partial \widetilde{\theta}}{\partial t} + \widetilde{u}_j \frac{\partial \widetilde{\theta}}{\partial x_j} = -\frac{\partial q_j}{\partial x_j} \ , \tag{3}$$

where the tilde ($\widetilde{\ }$) represents a spatial filtering at scale $\widetilde{\Delta}$, $(u_1, u_2, u_3) = (u, v, w)$ are the components of the velocity field (u is the component in the axial or x-direction, v is the component in the lateral or y-direction, and w is the component in the vertical or z-direction), $\widetilde{\theta}$ is the resolved potential temperature, θ_0 is the reference temperature, the angle brackets represent a horizontal average, g is the gravitational acceleration, f_c is the Coriolis parameter, δ_{ij} is the Kronecker

delta, ε_{ijk} is the alternating unit tensor, $\widetilde{p}^*$ is the effective pressure, and $\mathcal{F}_i$ is a forcing term (e.g., wind-turbine induced forces). The SGS stress and the SGS heat flux are defined as

$$\tau_{ij} = \widetilde{u_i u_j} - \widetilde{u}_i \widetilde{u}_j \,, \qquad q_j = \widetilde{u_j \theta} - \widetilde{u}_j \widetilde{\theta} \,. \tag{4}$$

Molecular dissipation and diffusion have been neglected since the Reynolds number is usually above $O(10^8)$. No near-ground viscous processes are resolved.

2.2 Scale-dependent Lagrangian dynamic models

A common parameterization approach in LES consists of computing the deviatoric part of the SGS stress with an eddy-viscosity model

$$\tau_{ij} - \frac{1}{3}\tau_{kk}\delta_{ij} = -2\nu_{sgs}\widetilde{S}_{ij} \,, \tag{5}$$

and the SGS heat flux with an eddy-diffusivity model

$$q_j = -\frac{\nu_{sgs}}{Pr_{sgs}} \frac{\partial \widetilde{\theta}}{\partial x_j} \,, \tag{6}$$

where $\widetilde{S}_{ij} = (\partial \widetilde{u}_i/\partial x_j + \partial \widetilde{u}_j/\partial x_i)/2$ is the resolved strain rate tensor, ν_{sgs} is the SGS eddy viscosity and Pr_{sgs} is the SGS Prandtl number. A popular way of modeling the eddy viscosity is to use the mixing length approximation [40]. As a result, the eddy viscosity is modeled as $\nu_{sgs} = C_s^2 \widetilde{\Delta}^2 |\widetilde{S}|$, where $|\widetilde{S}| = \left(2\widetilde{S}_{ij}\widetilde{S}_{ij}\right)^{1/2}$ is the strain rate and C_s is the Smagorinsky coefficient. When applied to calculating the SGS heat flux, the resulting eddy-diffusion model requires the specification of the lumped coefficient $C_s^2 Pr_{sgs}^{-1}$.

One of the main challenges in the implementation of the eddy-viscosity/diffusivity models is the specification of the model coefficients. The value of the model coefficients C_s and Pr_{sgs} (and therefore $C_s^2 Pr_{sgs}^{-1}$) is well established for isotropic turbulence. In that case, if a cut-off filter is used in the inertial subrange and the filter scale $\widetilde{\Delta}$ is equal to the grid size, then $C_s \approx 0.17$ and red$Pr_{sgs} \approx 0.5$ [41, 42]. However, anisotropy of the flow, particularly the presence of a strong mean shear near the surface in high-Reynolds-number ABLs, makes the optimum value of those coefficients depart from their isotropic counterparts [43, 44, 45]. A common practice is to specify the coefficients in an *ad-hoc* fashion. For C_s, this typically involves the use of dampening functions and stability corrections based on model performance and field data [46, 47, 43, 44]. Similarly, a stability dependence is usually prescribed for the SGS Prandtl number, for example, $Pr_{sgs} = 0.44$ under free convection and increasing to 1 for very stable stratification [48].

An alternative was introduced by Germano et al. [49] in the form of the dynamic Smagorinsky model, in which C_s is calculated based on the resolved flow field using a test filter ($\overline{f}$) at scale $\overline{\Delta} = \alpha\widetilde{\Delta}$ (with typically $\alpha = 2$). This procedure was also applied to the rededdy-diffusivity model by Moin et al. [50] to calculate the lumped coefficient. While the dynamic model removes the need for prescribed stability and shear dependence, it assumes that the model coefficients are scale invariant. Simulations (see Fig. 10 in Porté-Agel et al. [24], and Fig. 8 in Porté-Agel [36]) and experiments [51, 45] have shown that the scale invariance assumption breaks down near the surface, where the filter or test filter scales fall outside of the inertial subrange of the turbulence, and the assumption of a power-law dependence holds well for the SGS model coefficients.

The assumption of scale invariance in the standard dynamic model was relaxed through the development of scale-dependent dynamic models [24, 36] for the SGS stress and flux, respectively. In this study, we employ the recently developed scale-dependent Lagrangian dynamic models [25, 26] to compute the local optimized value of the model coefficients C_s and Pr_{sgs}. Based on the Germano identity [49, 52], the procedure of minimizing the error associated with the use of the model equations (5) and (6) results in the following equations

$$C_s^2(\widetilde{\Delta}) = \frac{\langle L_{ij} M_{ij} \rangle_{\mathcal{L}}}{\langle M_{ij} M_{ij} \rangle_{\mathcal{L}}}\,, \qquad C_s^2 Pr_{sgs}^{-1}(\widetilde{\Delta}) = \frac{\langle K_i X_i \rangle_{\mathcal{L}}}{\langle X_i X_i \rangle_{\mathcal{L}}}\,, \tag{7}$$

where $< \ldots >_{\mathcal{L}}$ denotes Lagrangian averaging [53, 25], and

$$L_{ij} = \overline{\widetilde{u}_i \widetilde{u}_j} - \overline{\widetilde{u}}_i \overline{\widetilde{u}}_j \;, \qquad M_{ij} = 2\widetilde{\Delta}^2 \left(\overline{|\widetilde{S}| \widetilde{S}_{ij}} - \alpha^2 \beta |\overline{\widetilde{S}}| \overline{\widetilde{S}}_{ij} \right) \;, \tag{8}$$

$$K_i = \overline{\widetilde{u}\widetilde{\theta}} - \overline{\widetilde{u}}_i \overline{\widetilde{\theta}} \;, \qquad \text{and } X_i = \widetilde{\Delta}^2 \left(\overline{|\widetilde{S}| \frac{\partial \widetilde{\theta}}{\partial x_i}} - \alpha^2 \beta_\theta |\overline{\widetilde{S}}| \frac{\partial \overline{\widetilde{\theta}}}{\partial x_i} \right) \;. \tag{9}$$

Here, $\beta = C_s^2(\alpha\widetilde{\Delta})/C_s^2(\widetilde{\Delta})$ is the ratio of C_s^2 at the test-filter scale and the filter scale, and $\beta_\theta = C_s^2 Pr_{sgs}^{-1}(\alpha\widetilde{\Delta})/C_s^2 Pr_{sgs}^{-1}(\widetilde{\Delta})$ is the ratio of $C_s^2 Pr_{sgs}^{-1}$ at the test-filter scale and the filter scale. Instead of assuming $\beta = 1$ and $\beta_\theta = 1$ as scale-invariant models do, the scale-dependent Lagrangian dynamic models leave the two parameters as unknowns that will be calculated dynamically. The implementation requires use of a second test filter ($\widehat{f}$) at scale $\widehat{\Delta} = \alpha^2\widetilde{\Delta}$. In addition, the models assume a power-law dependence of the coefficients with scale, and thus

$$\beta = \frac{C_s^2(\alpha\widetilde{\Delta})}{C_s^2(\widetilde{\Delta})} = \frac{C_s^2(\alpha^2\widetilde{\Delta})}{C_s^2(\alpha\widetilde{\Delta})}\,, \qquad \beta_\theta = \frac{C_s^2 Pr_{sgs}^{-1}(\alpha\widetilde{\Delta})}{C_s^2 Pr_{sgs}^{-1}(\widetilde{\Delta})} = \frac{C_s^2 Pr_{sgs}^{-1}(\alpha^2\widetilde{\Delta})}{C_s^2 Pr_{sgs}^{-1}(\alpha\widetilde{\Delta})}\,. \tag{10}$$

It is important to note that this assumption is much weaker than the assumption of scale invariance ($\beta = 1$ and $\beta_\theta = 1$) in scale-invariant models, such as the dynamic Smagorinsky model, and has been shown to be more realistic in recent *a-priori* field studies [45]. Again minimizing the error associated with the use of the model equations (5) and (6), another set of equations for C_s and Pr_{sgs} are

$$C_s^2(\widetilde{\Delta}) = \frac{\left\langle L'_{ij} M'_{ij} \right\rangle_{\mathcal{L}}}{\left\langle M'_{ij} M'_{ij} \right\rangle_{\mathcal{L}}}\,, \qquad C_s^2 Pr_{sgs}^{-1}(\widetilde{\Delta}) = \frac{\langle K'_i X'_i \rangle_{\mathcal{L}}}{\langle X'_i X'_i \rangle_{\mathcal{L}}}\,, \tag{11}$$

where

$$L'_{ij} = \widehat{\widetilde{u}_i \widetilde{u}_j} - \widehat{\widetilde{u}}_i \widehat{\widetilde{u}}_j \;, \qquad M'_{ij} = 2\widetilde{\Delta}^2 \left(\widehat{|\widetilde{S}| \widetilde{S}_{ij}} - \alpha^4 \beta^2 |\widehat{\widetilde{S}}| \widehat{\widetilde{S}}_{ij} \right) \;, \tag{12}$$

$$K'_i = \widehat{\widetilde{u}\widetilde{\theta}} - \widehat{\widetilde{u}}_i \widehat{\widetilde{\theta}} \;, \qquad \text{and } X'_i = \widetilde{\Delta}^2 \left(\widehat{|\widetilde{S}| \frac{\partial \widetilde{\theta}}{\partial x_i}} - \alpha^4 \beta_\theta^2 |\widehat{\widetilde{S}}| \frac{\partial \widehat{\widetilde{\theta}}}{\partial x_i} \right) \;. \tag{13}$$

More details can be found in Porté-Agel et al. [24], Porté-Agel [36], and Stoll and Porté-Agel [25, 26].

Tests of different averaging procedures (over horizontal planes, local and Lagrangian) and simulations of a stable boundary layer with the scale-dependent dynamic model have shown that

Lagrangian averaging produces the best combination of self-consistent model coefficients, first- and second-order flow statistics, and small sensitivity to grid resolution [26]. Based on the local dynamics of the resolved scales, these tuning-free models compute C_s and Pr_{sgs} dynamically as the flow evolves in both space and timered. Hence, they are well suited for ABL flows associated with inhomogeneities.

2.3 Wind-turbine parameterization

Figure 1(a) shows a typical three-blade horizontal axis upwind wind turbine, which usually exhibits much better power efficiency than other types of wind turbines [54]. The actuator line method [32, 33, 34] combines a three-dimensional flow solver with a technique in which body forces are distributed radially along lines, which represent the blades of the wind turbine.

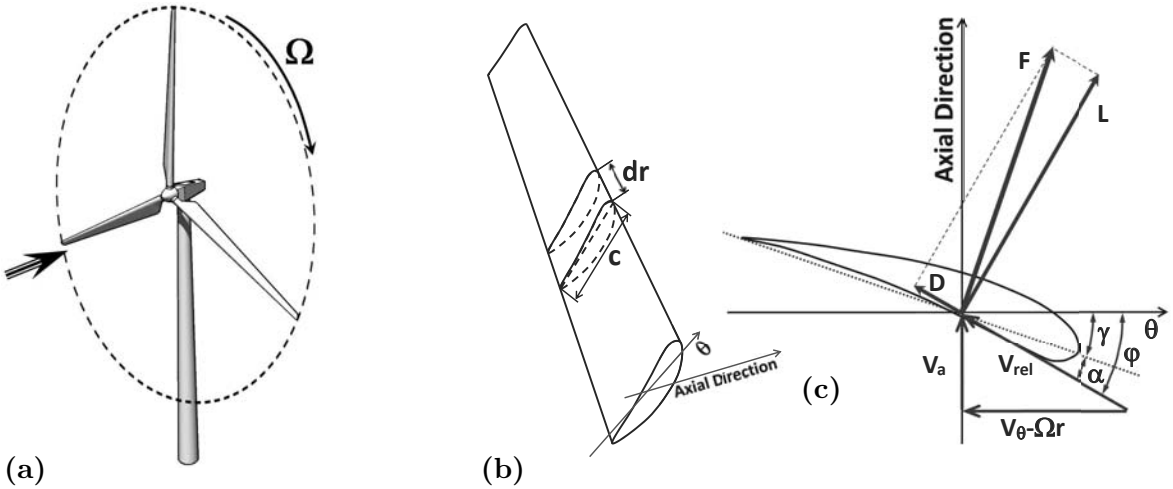

Figure 1: Schematic of the actuator line model: (a) three-dimensional view of a wind turbine; (b) a discretized blade; and (c) cross-section airfoil element showing velocities and force vectors.

Figure 1(b) shows one discretized element of a blade, and figure 1(c) shows a cross-sectional element at radius r defining the airfoil in the (θ, x) plane, where x is the axial direction. With the tangential and axial velocities of the incident flow denoted as V_θ and V_a, respectively, the local velocity relative to the rotating blade is given as $\mathbf{V}_{rel} = (V_\theta - \Omega r, V_a)$. The angle of attack is defined as $\alpha = \varphi - \gamma$, where $\varphi = tan^{-1}(V_a/(\Omega r - V_\theta))$ is the angle between $\mathbf{V}_{rel}$ and the rotor plane, and γ is the local pitch angle. The turbine-induced force per radial unit length is given by the following equation

$$\mathbf{f} = \frac{\mathbf{dF}}{dr} = \frac{1}{2}\rho V_{rel}^2 c(C_L \mathbf{e}_L + C_D \mathbf{e}_D) \ , \tag{14}$$

where $C_L = C_L(\alpha, Re)$ and $C_D = C_D(\alpha, Re)$ are the lift coefficient and the drag coefficient, respectively, ρ is the air density, c is the chord length, and $\mathbf{e}_L$ and $\mathbf{e}_D$ denote the unit vectors in the directions of the lift and the drag, respectively. The flow of interest is essentially inviscid, and viscous effects from the boundary layer of blade are introduced only as integrated quantities through the use of airfoil data. The airfoil data and subsequent loading are determined by computing local angles of attack from the movement of the blades and the local flow field. The model enables us to study in detail the dynamics of the wake and the tip vortices and their

influence on the induced velocities in the rotor plane. The applied blade forces are distributed smoothly to avoid singular behavior and numerical instability. In practice, the aerodynamic blade forces are distributed along and away from the actuator lines in a three-dimensional Gaussian manner through the convolution of the computed local load, $\mathbf{f}$, and a regularization kernel η_ϵ as shown below

$$\mathbf{f}_\epsilon = \mathbf{f} \otimes \eta_\epsilon \,, \qquad \eta_\epsilon = \frac{1}{\epsilon^3 \pi^{3/2}} \exp\left(-\frac{d^2}{\epsilon^2}\right) \,, \tag{15}$$

where d is the distance between grid points and points at the actuator line, and ϵ is a parameter that serves to adjust the concentration of the regularized load. The value of this regularization parameter, ϵ, is typically on the order of $1-3$ grid sizes and should be as small as possible so that the turbine-induced force is distributed over an area representing the chord distribution and does not affect the wake structure. However, small values will deliver significant numerical oscillations; thus, as a trade-off between numerical stability and accuracy [55, 34], we set it as 1.5 times of the grid size in the rotor plane. Validation of the LES of wind-turbine wakes using the ALM has been performed using experimental measurements from the wind tunnel at Saint Anthony Falls Laboratory/University of Minnesota, and ABL field measurements in an operational wind farm located in Mower County, Minnesota (more details can be found in Wu and Porté-Agel [56] and Porté-Agel et al. [57]).

The main advantage of representing the blades by airfoil data is that many fewer grid points are needed to capture the influence of the blades than would be needed for simulating the actual geometry of the blades. Therefore, the ALM is well suited for wake studies since grid points can be concentrated in a larger part of the wake while keeping the computing costs at a reasonable level. redMoreover, the ALM encompasses blade motions as well as their mixing mechanism, which is crucial for simulating more realistic wind-turbine wakes and achieving improved predictions with respect to the standard actuator disk model [3, 56, 57]. However, the ALM does not resolve detailed flows on blade surfaces and relies on tabulated two-dimensional airfoil data for providing redlift and drag coefficients. This makes it dependent on both the quality of airfoil data and the method used to model the influence of dynamically changing angles of attack and stall. We note that the ALM employs the two-dimensional airfoil theory to provide the basis for the incident flow velocity for computing lift and drag forces, and the local air velocity should not be exactly the same as the incident velocity. To correct the inflow, in this study we have adopted an induction factor technique (sometimes referred to as "inflow factor" or "interference factor" [58, 59]), which is crucial to the improvement of simulation accuracy [56, 57]. Basically, the BEM theory equates different methods of examining how a wind turbine operates, such as a momentum balance on a rotating annular stream tube passing through a turbine, the self-induction from the local bound circulation, and the lift and drag forces generated by the airfoil at various sections along the blades. These methods then provide a series of equations that can be solved iteratively to determine the angle of attack and compute the inflow velocity [60].

3 Simulation details

In order to reduce uncertainties when studying the effects of a wind farm on a SBL, it is important to start with a SBL case (without wind turbines) that has been well established and tested with LES. Such case was launched for an LES inter-comparison study as part of the Global Energy and Water Cycle Experiment Atmospheric Boundary Layer Study (GABLS) initiative [61]. It

represents a typical quasi-equilibrium moderately SBL, similar to those commonly observed over polar regions and equilibrium nighttime conditions over land in mid-latitudes.

Figure 2(a) shows a schematic of the computational domain. In order to study the effect of a wind farm on the GABLS case, we have "immersed" a wind turbine of similar characteristics to the V112-3.0MW in the GABLS domain such that the wind-turbine center is located at $x_c = 80\,\mathrm{m}$, $y_c = 280\,\mathrm{m}$, and $z_c = 119\,\mathrm{m}$ (hub-height). This wind turbine has a rotor diameter of $D = 112\,\mathrm{m}$ (rotor radius $R = D/2 = 56\,\mathrm{m}$), and rotates at 8 RPM, corresponding to a tip speed ratio of approximately 7 for an optimal performance at a free-stream wind speed of approximately 6 m/s. The blade length is 54.6 m, and the blades consist of the Risø-A1-18 airfoil, which has the same design objectives as those for the Risø-P-18 airfoil [62]. For simplicity, we adopt a linear chord distribution from 4 m at the blade root to 0.5 m at the tip, and a linear twist distribution from 17.5° at the blade root to 0° at the tip. The nacelle is modeled as a bullet-shaped object ($C_d = 0.3$) in high Reynolds number turbulent flow. The tower shadow could also be simulated with a distribution of energy sinks; however, as the frontal area of the tower is much smaller than that of the rotor, the effects of the tower are not considered in this study. In the current scenario, the top-tip height is 175 m, which is similar to the SBL height of the baseline case.

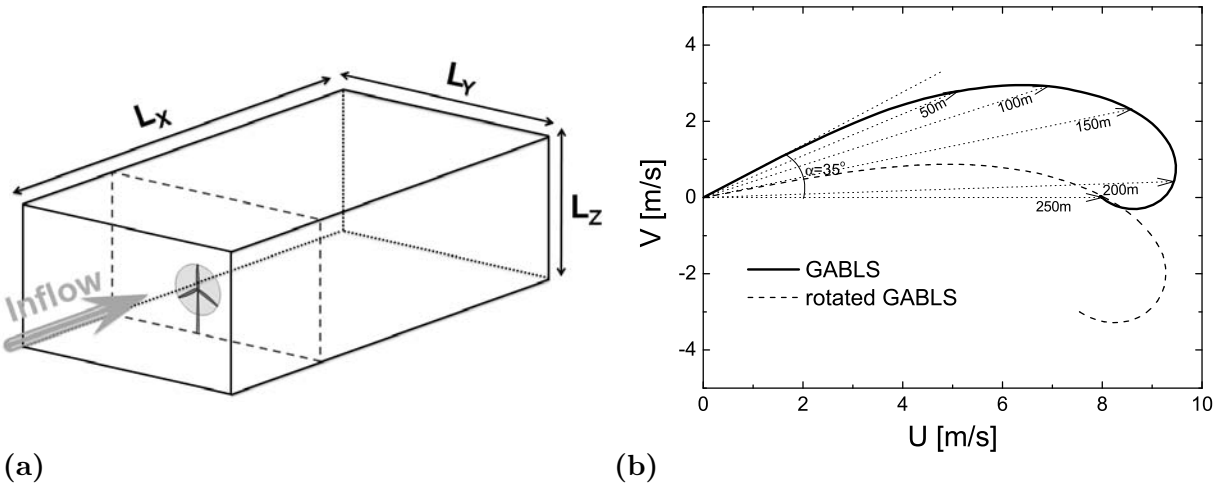

Figure 2: (a) Schematic of the computational domain with a wind-turbine model; and (b) Ekman spiral of the GABLS case.

Periodic boundary conditions are applied horizontally so that an infinitely large wind farm can be simulated. The horizontal directions are discretized pseudo-spectrally, and vertical derivatives are approximated with second-order central differences. As in the original GABLS case, the vertical height of the computational domain is $L_z = 400\,\mathrm{m}$. The domain size in the y-direction is fixed to be $L_y = 5D = 560\,\mathrm{m}$, and two x-direction dimensions, corresponding to two typical wind-turbine spacings, are studied: (i) $L_x = 8D = 896\,\mathrm{m}$ (the corresponding LES is abbreviated as the 8D case); (ii) $L_x = 5D = 560\,\mathrm{m}$ (the corresponding LES is abbreviated as the 5D case). The domain is divided into N_x, N_y, and N_z uniformly spaced grid points and simulations are carried out with the resolution of $N_x \times N_y \times N_z = 270 \times 168 \times 120$ for the 8D case and $N_x \times N_y \times N_z = 168 \times 168 \times 120$ for the 5D case. The statistics of several GABLS simulations are stationary with increasing resolution when the grid size is below $\approx 3\,\mathrm{m}$ [61]. We note that Stoll and Porté-Agel [26] have shown that satisfactory GABLS results can be achieved for a grid size of $\approx 6\,\mathrm{m}$

or less ($N_z \geq 64$) when the scale-dependent Largangian dynamic models are adopted. Also, we have performed a grid convergence study at a coarser (1/3 fewer points in each direction) resolution. The results are found to depend only mildly (not shown here) on the grid resolutions under consideration. The grid planes are staggered in the vertical with the first vertical velocity plane at a distance $\Delta z = L_z/(N_z - 1)$ from the surface, and the first horizontal velocity plane $\Delta z/2$ from the surface. The filter width is computed according to the common formulation $\widetilde{\Delta} = (\Delta x\, \Delta y\, \Delta z)^{1/3}$, where $\Delta x = L_x/N_x$ and $\Delta y = L_y/N_y$. The corresponding aliasing errors are corrected in the nonlinear terms according to the 3/2 rule [63]. The time advancement takes place according to a second-order-accurate Adams-Bashforth scheme [63]. We set a constant time-step of $\approx 0.018\,\mathrm{s}$ corresponding to a rather restrictive Courant-Friedrichs-Lewy number of ≈ 0.06 to suppress the error from the time stepping.

At the bottom surface, the instantaneous wall stress is related to the velocity at the first vertical node through the application of the Monin-Obukhov similarity theory [64]. Although this theory was developed for mean quantities, it is common practice [37, 38, 26] in LES of atmospheric flows to use it for instantaneous fields as follows

$$\tau_{i3}|_w = -u_*^2 \frac{\widetilde{u}_i}{u_r} = -\left(\frac{u_r\,\kappa}{\ln\left(z/z_0\right) - \Psi_M}\right)^2 \frac{\widetilde{u}_i}{u_r} \qquad (i = 1,\ 2)\ , \tag{16}$$

where $\tau_{i3}|_w$ is the instantaneous local wall stress, u_* is the friction velocity, $z_0 = 0.1\,\mathrm{m}$ is the roughness length, κ is the von Kármán constant, Ψ_M is the stability correction for momentum, and u_r is the local filtered horizontal velocity at the first vertical level ($z = \Delta z/2$). In a similar manner, the surface heat flux is computed as

$$q_3|_w = \frac{u_* \kappa \left(\theta_s - \widetilde{\theta}\right)}{\ln\left(z/z_0\right) - \Psi_H}\ , \tag{17}$$

where θ_s is the surface (ground level) potential temperature, and $\widetilde{\theta}$ denotes the resolved potential temperature at the first vertical level. Following the recommendations of the GABLS intercomparison study, we adopt $\kappa = 0.4$, $\Psi_M = -4.8\frac{z}{L}$ and $\Psi_H = -7.8\frac{z}{L}$ (where $L = -\frac{u_*^3 \widetilde{\theta}}{\kappa g q_3|_w}$ is the local Obukhov length) in this study. The upper boundary condition is a stress-free/flux-free condition. A Rayleigh damping layer at 300 m is used following the GABLS case description. Simulations show the maximum SBL height is about 250 m (see later in subsection 4.1). It is less than the maximum SBL heights (grid dependence is the primary cause [65]) of a few cases reported in Beare et al. [61], which did not show any wave reflection from the top. We confirm that, in the current scenario, the damping layer is still capable of limiting gravity-wave reflection from the top of the domain; however, further developments might require some more vertical space for a proper simulation of the phenomenon.

The GABLS LES intercomparison case study is described in detail by Beare et al. [61]. In this study, we have simulated a complete GABLS case as the "baseline" case (no-turbine case) based on the description. In summary, the boundary layer is driven by an imposed, uniform geostrophic wind of 8 m/s; the Coriolis parameter is set to $f_c = 1.39 \times 10^{-4}\,\mathrm{rad/s}$, corresponding to latitude 73°; the initial potential temperature profile consists of a mixed layer (with potential temperature 265 K) up to 100m with an overlying inversion of strength 0.01 K/m, and the surface (ground level) potential temperature is reduced at a prescribed surface cooling rate of 0.25 K/h.

It should be noted that the baseline case attains a quasi-steady state in 8 - 9 h [61]. Therefore, in order to examine the wind-turbine effects relative to the baseline case, we introduce the wind turbines only in the last hour of simulation. The initial velocity and temperature profiles are taken at 8 h, and we align the mean velocity direction to be axial at the hub-height level (rotated approximately 20° as shown in Fig. 2(b)).

4 Results

The simulations performed here provide high-resolution three-dimensional fields of velocity and temperature in the boundary layer. This section compare simulation results obtained with and without wind turbines. Special emphasis is placed on studying the structure of wind-turbine wakes, as well as their overall effect on the area-averaged momentum and heat fluxes in the SBL. In the presentation, we denote the horizontal and time average as $< \ldots >$, and the time average as $< \ldots >_t$.

4.1 Temporal measures

Figure 3 shows the time series of the stable boundary-layer height, the surface momentum flux (based on Eqn. 16) and the surface buoyancy flux (based on Eqn. 17). Data are sampled approximately every 10 seconds, and averaging is taken over horizontal planes. Following Kosovic and Curry [66] and Beare et al. [61], the SBL height is defined as (1/0.95) times the height where the horizontally averaged stress falls to five percent of its surface value. The baseline case results are in good agreement with other GABLS simulation studies [61, 38, 26]. It remains in its quasi-equilibrium state within this last hour. The mean SBL height is approximately 175 m; at the surface, the magnitude of the mean momentum flux is approximately $0.072\,\mathrm{m}^2/\mathrm{s}^2$, corresponding to a friction velocity of 0.27 m/s, and the mean buoyancy flux is approximately $-4.3\times10^{-4}\,\mathrm{m}^2/\mathrm{s}^3$, corresponding to a heat flux of $-15.7\,\mathrm{W/m}^2$.

Figure 3(a) shows that, when wind turbines are installed, there exists a significant increase of the boundary-layer height, which is associated with the wake expansion. Specifically, over the last 15 min, the 8D case yields a SBL height of approximately 225 m (increased $\approx$ 28%), and the 5D case yields a SBL height of approximately 250 m (increased $\approx$ 43%). The current simulation results support the tendency that smaller wind-turbine spacing yields larger boundary-layer increases. The increase of the boundary-layer height happens very quickly after the time when the wind turbines are immersed. This is due to the formation and expansion of the turbine wakes, which occurs radially (both laterally and vertically).

Figures 3(b) and 3(c) show declines in the magnitudes of the surface momentum flux and the surface buoyancy flux. Specifically, over the last 15 min, the 8D case yields a momentum-flux magnitude of approximately $0.05\,\mathrm{m}^2/\mathrm{s}^2$ (reduced $\approx$ 30%), corresponding to a friction velocity of 0.23 m/s; the 5D case yields a momentum-flux magnitude of approximately $0.043\,\mathrm{m}^2/\mathrm{s}^2$ (reduced $\approx$ 40%), corresponding to a friction velocity of 0.21 m/s. The 8D case yields a buoyancy-flux magnitude of approximately $-3.8\times10^{-4}\,\mathrm{m}^2/\mathrm{s}^3$ (reduced $\approx$ 15%), corresponding to a heat flux of $-13.5\,\mathrm{W/m}^2$; the 5D case yields a buoyancy-flux magnitude of approximately $-3.2\times10^{-4}\,\mathrm{m}^2/\mathrm{s}^3$ (reduced $\approx$ 28%), corresponding to a heat flux of $-11.4\,\mathrm{W/m}^2$. It is interesting to note that it takes some time before wind turbines are able to affect surface fluxes. This delay in the change of the fluxes is likely associated to the time it takes for the multiple wakes to expand horizontally

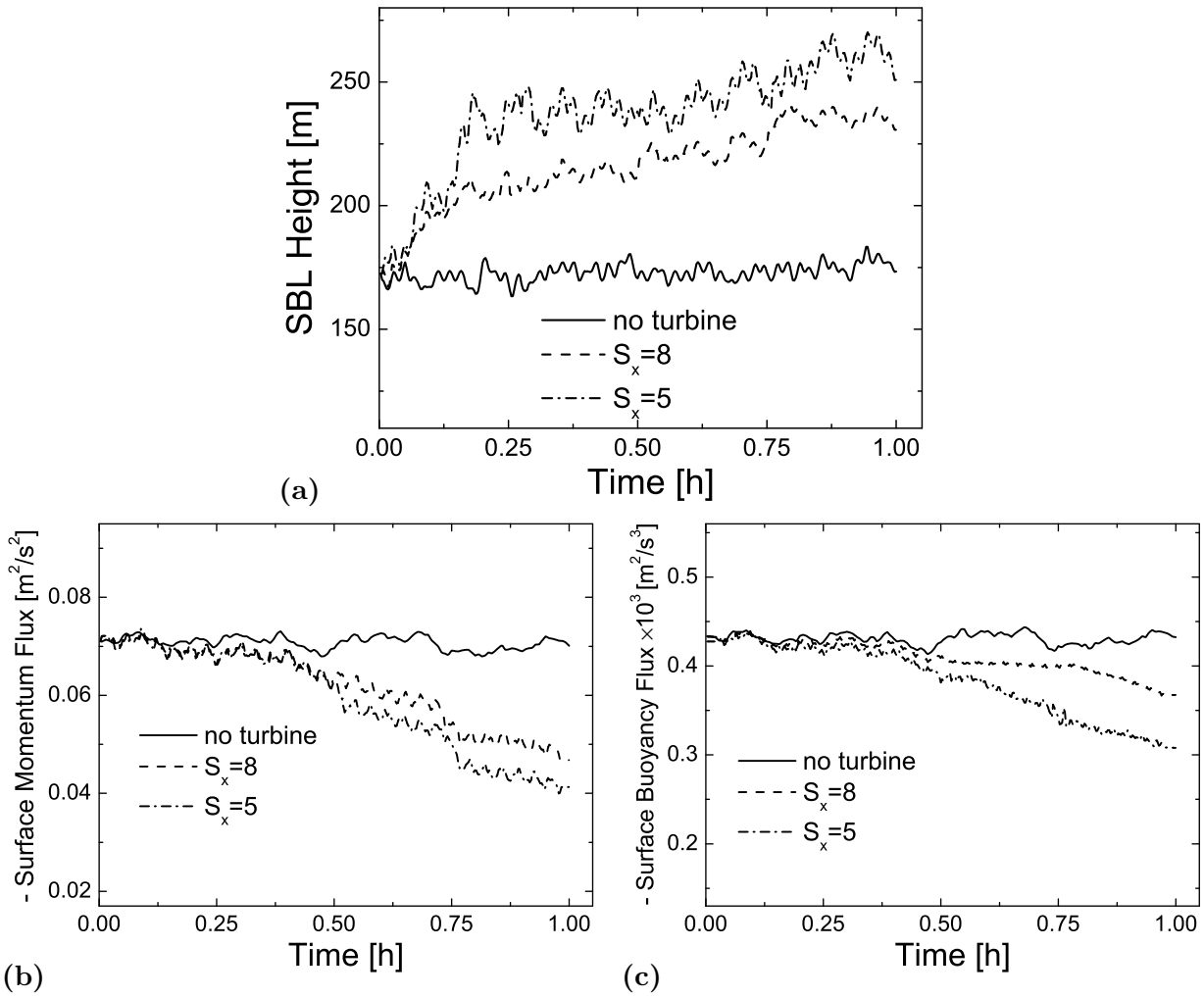

Figure 3: (a) Evolution of stable boundary-layer height; (b) evolution of surface momentum flux; and (b) evolution of surface buoyancy flux. Solid lines: results obtained from the baseline case; dashed lines: results obtained from the 8D case; dash dotted lines: results obtained from the 5D case.

and affect the entire surface area. Overall, the reduced surface heat flux phenomenon obtained from the current research is consistent with the results from low-resolution wind-farm simulations performed by Baidya Roy et al. [3]. The reduced surface momentum and heat flux magnitudes indicate a reduction in the level of turbulent mixing and transport near the surface. Regarding the overall thermal-energy budget, this reduced heat flux is consistent with the increase of air temperature in the boundary layer, as shown later in subsection 4.3.

4.2 Tip vortices and tangential velocities

As mentioned before, one of the key advantages of using the actuator line model in LES is that, by computing and distributing the blade-induced forces radially along each of the rotor blades, it enables to capture important vortical structures such as helicoidal tip vortices. In contrast,

actuator disk models distribute the forces evenly over the rotor disk (the entire area swept by the blades) and, consequently cannot produce such vortices.

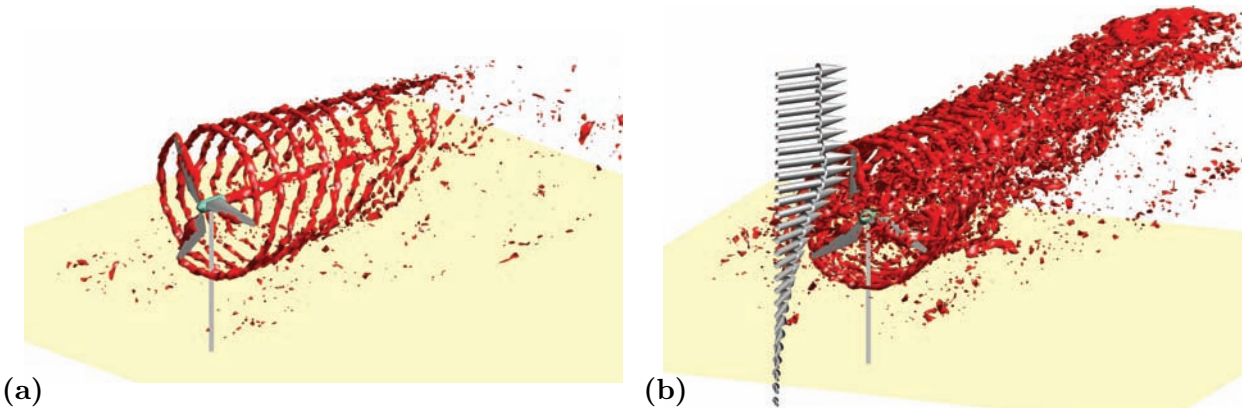

Figure 4: Iso-surface of vorticity showing the three-dimensional structures of an instantaneous field at different moments in the 5D case: (a) at $t = 30\,\mathrm{s}$; (b) at $t = 150\,\mathrm{s}$. redA movie showing the time evolution of the instantaneous wake velocity and the tip-vortex structure is available in the supplementary material [67].

Figure 4 shows the blade-induced three-dimensional helicoidal tip vortices detected in the 5D case by means of $|\omega|$-definition (approximately 0.3 times the maximum vorticity [68]). The mean velocity vectors are presented in front of the wind turbine in figure 4(b), illustrating the change in wind direction produced by the Coriolis effect. Figure 4(a) shows the formation (initial stages) of tip vortices. Owing to the strong shear and the non-uniformity of the incoming boundary-layer flow, helicoidal vortices are stretched as they travel faster at the top tip level, in contrast to the bottom tip level. The stretch advances to break up the tip vortices. Approximately, the flow takes 100 seconds to travel through the whole axial distance. Figure 4(b) shows general vortex structures after passing the initial transition period. The previous blade-induced flows become the inflow of the next wind turbine, thus, more complex turbulent structures are formed.

When the fluid applies torque to the rotor, as a reaction, a tangential (to the rotor) velocity component is generated behind the rotor [69]. Present results show that the ALM redis able to capture the rotational wake structure. The time-averaged (over the last 15 min) vertical velocity contours on the horizontal plane at the hub height are plotted in figure 5(a), and the extracted data in figure 5(b) are taken at the rotor position and 1D downwind of the rotor position, respectively. It is readily seen that the wake is slowly expanding and that the averaged tangential velocity approximately follows a 1/r relationship, as expected from classical theory. The exact profile should be dependent on turbulence as well as the details of the blade, such as chord length, pitch angle, and airfoil. The maximum magnitude of the tangential velocity at the rotor position is approximately $0.6\,\mathrm{m/s}$, which is approximately 10% of the incoming axial velocity. These results are consistent with redanother simulation study [34]. Principally caused by turbulent mixing, the tangential velocity magnitude decreases as downwind distance increases, and such a phenomenon has also been revealed in high-Reynolds-number experimental studies [69].

Further, figures 6(a) and 6(b) compare the kinetic-energy power spectra sampled at top-tip height and downwind distances of 0.5D and 3D, respectively; and figure 7 shows power spectra of

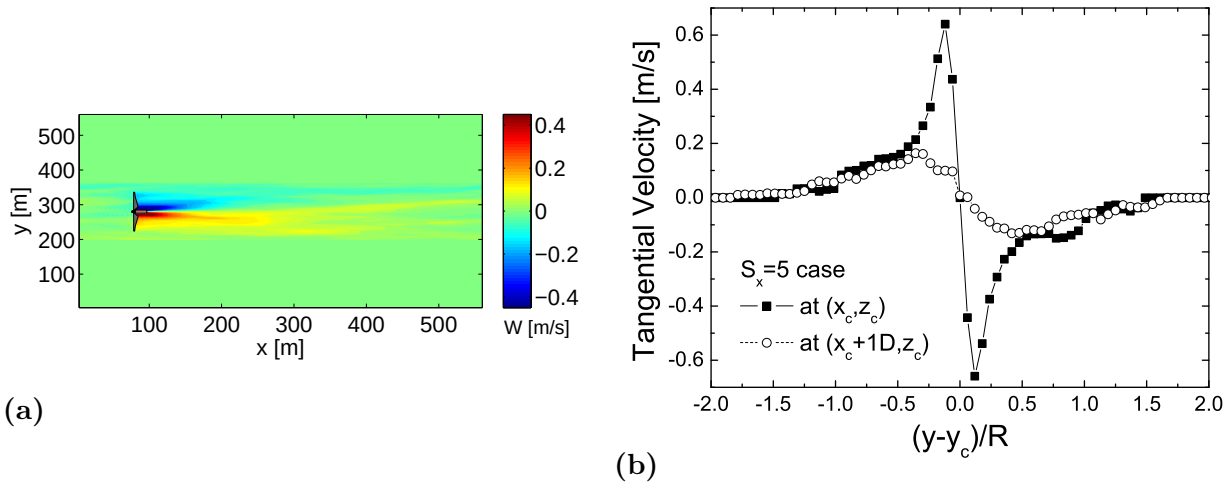

Figure 5: (a) Filled contours of time-averaged (over the last 15 min) vertical velocity on the x-y plane at the hub-height obtained from the 5D case; (b) extracted (from (a)) data as a function of radius at two different downwind positions.

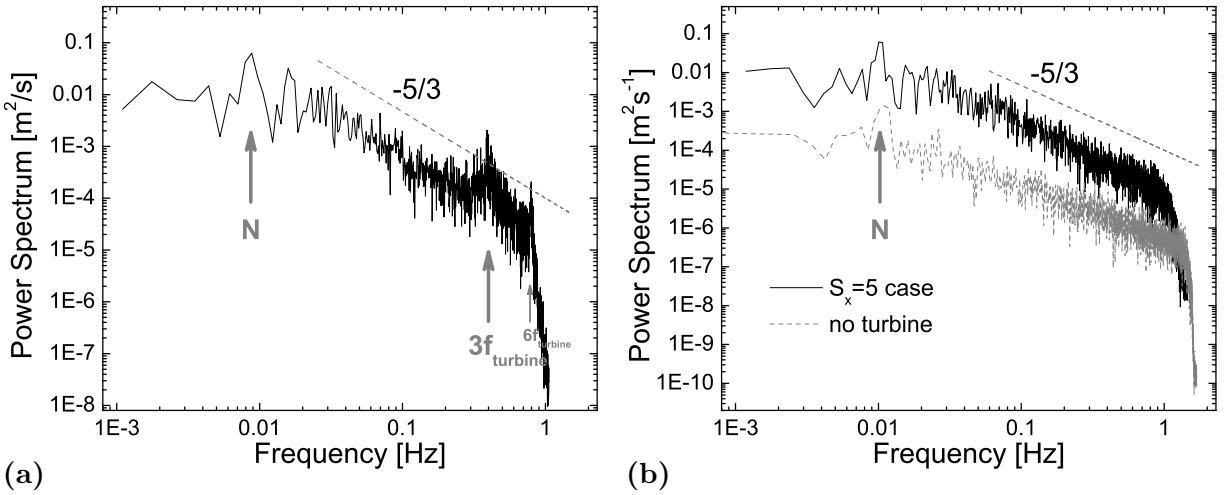

Figure 6: Kinetic-energy power spectrum sampled over the last 15 min of the 5D case: (a) at the location $(x_c + 0.5D, y_c, z_c + 0.5D)$; and (b) at the location $(x_c + 3D, y_c, z_c + 0.5D)$; spectrum obtained from the baseline case is shown as a gray dashed line.

different velocity components and potential temperature fluctuations in the near-wake region. In line with the experimental results of other studies [70], a clear peak, coinciding with three times the frequency of the rotor rotation (as well as its first resonant mode), appears only in the near-wake region. Also, the tip vortices leave a stronger signature in the vertical velocity spectrum compared to horizontal velocity components, and the temperature variance spectrum does not show a convincing evidence for the existence of tip vortices. Turbulence diffuses the energy to scales around this frequency, and then that spectral peak is not observable at longer distances, away from the near-wake region. Also, the peak can be observed further away at the top-tip height, compared with the bottom-tip height (not shown here). This effect is due to the fact that

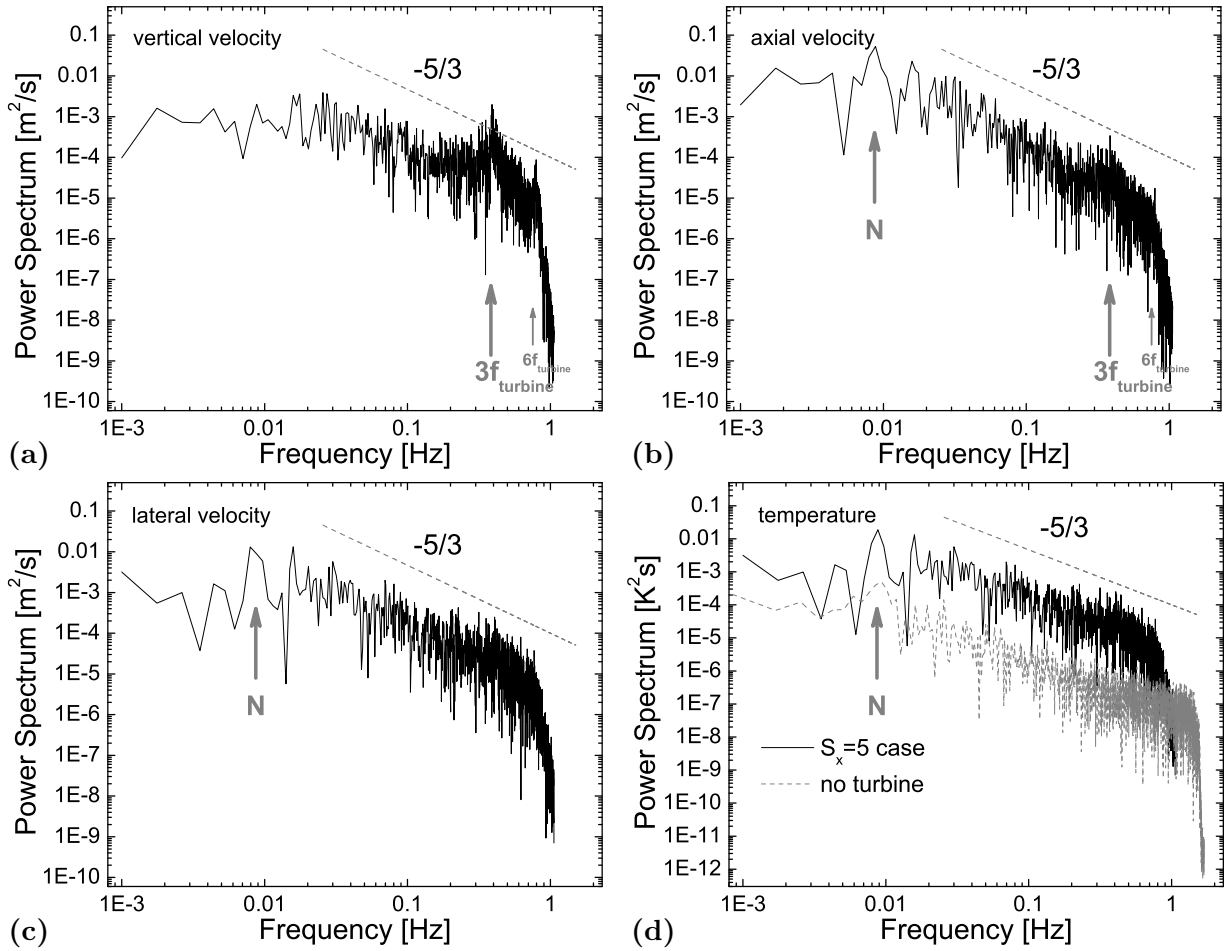

Figure 7: Power spectrum of different components sampled over the last 15 min of the 5D case at the location $(x_c + 0.5D, y_c, z_c + 0.5D)$; (a) vertical-velocity component, (b) axial-velocity component, (c) lateral-velocity component, and (d) potential temperature fluctuation; spectrum obtained from the baseline case is shown as a gray dashed line.

the wind turbine is placed in a shear flow as shown in figure 4(a), and it has been confirmed by experimental research [70]. The power spectra also show the buoyancy frequency (also known as the Brunt-Väisälä frequency), $N = \sqrt{\frac{g}{\theta_0}\frac{d<\widetilde{\theta}>}{dz}}$, as well as the $-5/3$ power law behavior in the inertial subrange. Section 4.4 will discuss the large-scale fluctuations in more detail. As expected, the power spectrum drops at a scale corresponding to the resolution of the LES. The smallest time scales, corresponding to a frequency on the order of hundreds of Hz, are not resolved. In LES, the increase of grid resolution will yield an extension of the resolved portion of the inertial subrange. Figures 6(b) and 7(d) also include power spectra obtained from the baseline case. Compared to the wind-turbine wake spectra, they yield similar scaling behaviors except that: (i) the inertial subranges extend slightly further since, as shown in section 4.3, the baseline case yields higher mean top-tip-height wind speed, which allows the simulation to resolve smaller time scales (proportional to the grid size divided by the mean wind speed); and (ii) their fluctuation

magnitudes are about 100 times smaller as shown later in section 4.6 through the comparison of turbulence levels at the top-tip height.

4.3 Mean velocities and temperature

Figure 8 shows the mean profiles of wind speeds and potential temperature obtained from the 8D case, the 5D case, and the baseline simulation. Averaging is performed both horizontally and in time (over the last 15 min). Consistent with other studies [61, 38, 26], the baseline case clearly shows a low-level jet peaking near the top of the boundary layer. Principally caused by energy transformation in the wind turbines, the 8D case and the 5D case do not show a clear jet, and the comparison reveals that a smaller distance between wind turbines results in more extraction of mean kinetic energy from the flow.

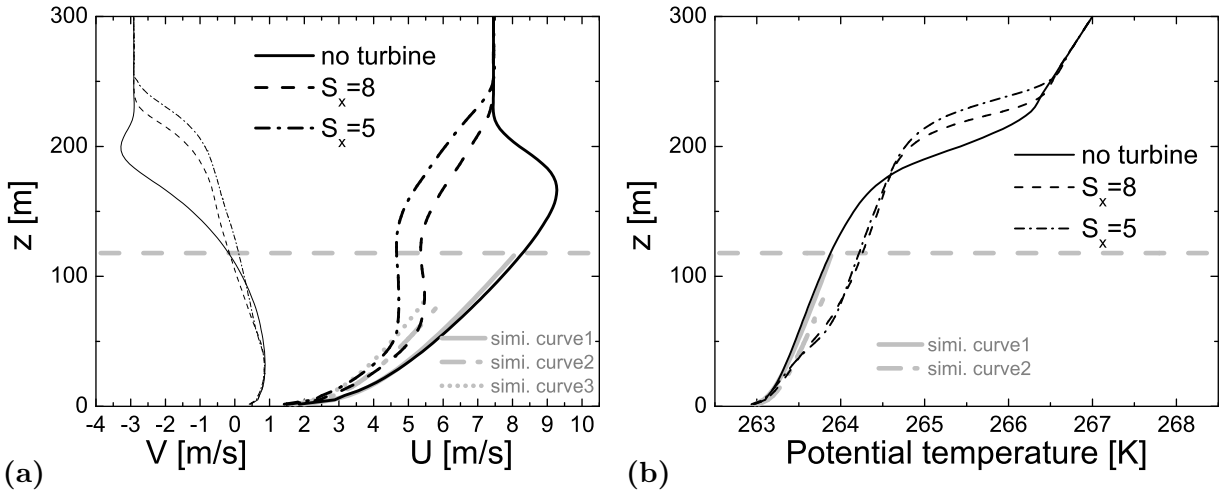

Figure 8: Vertical distributions of mean profiles: (a) x-direction velocity U (Bold) and y-direction velocity V; (b) potential temperature. Solid lines: results obtained from the baseline case; dashed lines: results obtained from the 8D case; dash-dotted lines: results obtained from the 5D case; gray lines: Monin-Obukhov similarity curves; horizontal gray dashed line: turbine hub height.

Based on the Monin-Obukhov similarity theory [64], the velocity profile in SBL can be formulated as $U(z) = \frac{u_*}{\kappa}\left(\ln\frac{z}{z_0} + 4.8\frac{z}{L}\right)$. The first similarity curve, which bears $u_* = 0.27\,\mathrm{m/s}$ and $L = 120\,\mathrm{m}$, shows that the similarity profile is satisfied properly in the near-wall region of the baseline case. Interestingly, the near-wall region velocity profiles obtained from the wind-turbine cases also exhibit the redsame type of similarity profile, which bears a lower turbulent friction velocity, $u_* = 0.23\,\mathrm{m/s}$ and $u_* = 0.21\,\mathrm{m/s}$, respectively, than -and the same Obukhov-length as- the baseline case. Regarding the potential temperature, the baseline case does satisfactorily yield a simple similarity temperature profile, $\Theta(z) = \Theta_s + 0.74\frac{\theta_*}{\kappa}\left(\ln\frac{z}{z_0} + 7.8\frac{z}{L}\right)$, with $\theta_* = 0.042\,\mathrm{K}$, and the two wind-turbine simulations deliver almost identical temperature profiles fitting a surface-layer similarity profile with $\theta_* = 0.045\,\mathrm{K}$. These findings suggest that boundary-layer turbulence below the blade bottom still satisfies Monin-Obukhov similarity theory, and that wind turbines act as a top boundary forcing on this region. Further, compared to the potential temperature profile from the baseline case as shown in figure 8(b), temperature drops between the top-tip

height and the SBL height and rises below the top-tip height by approximately 0.5 K. This is primarily because blade motions enhance vertical mixing (see section 4.7) and transfer more thermal energy from levels above the top-tip height to lower levels.

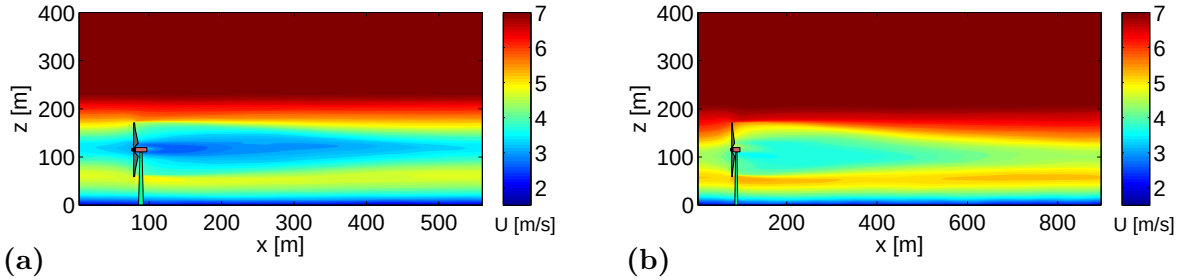

Figure 9: Filled contours of time-averaged (over the last 15 min) x-direction velocity on the x-z plane through the axis of the turbine: (a) the 5D case; (b) the 8D case.

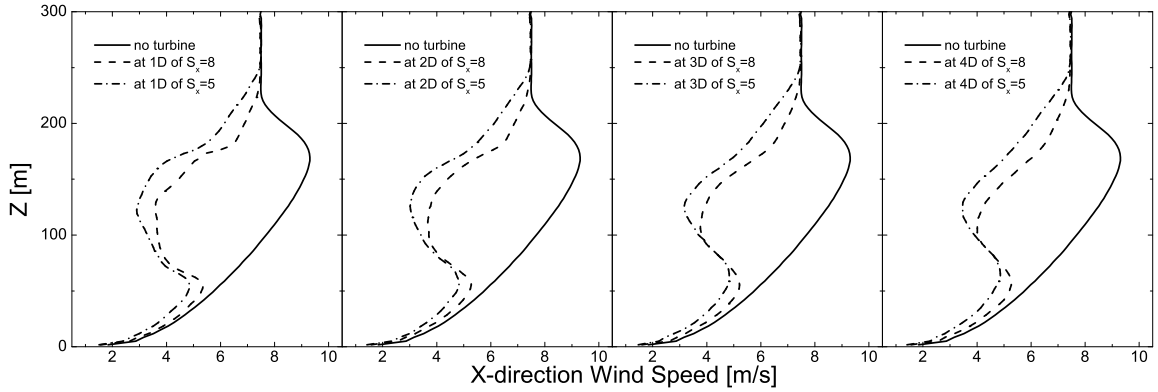

Figure 10: Vertical distribution of time-averaged (over the last 15 min) x-direction velocity obtained from the baseline case (solid), the 8D case (dashed), and the 5D case (dash dotted) through the axis of the turbine at different downwind locations.

To understand the flow structure inside and above the wind farm, it is important to investigate the detailed structure of the wind-turbine wakes. Figure 9 shows the filled contours of the time-averaged axial velocity on the x-z plane through the turbine axis. Furthermore, to facilitate a quantitative comparison, figure 10 shows vertical profiles of the time-averaged axial velocity for selected downwind locations ($x/D = 1, 2, 3$, and 4). Again, it is clear that a smaller distance between wind turbines results in more extraction of kinetic energy. Owing to the non-uniform inflow profile and the presence of the wall, the velocity distribution inside the turbine wake does not show axisymmetric behavior. Also observable is a slightly downward tilt of the wake centerline, which is consistent with wind-tunnel measurements and other simulation results summarized by Vermeer et al. [2]. Moreover, figure 11 shows the filled contours of the time-averaged axial velocity at different downwind positions. The view is from downwind. In line with recent simulations [71], it is evident that the axial-velocity deficit develops in a highly three-dimensional manner (highly asymmetric), caused by the combination of the mean flow direction changes, the wake rotation and the free stream transport velocity. Owing to the strong cross flow component the

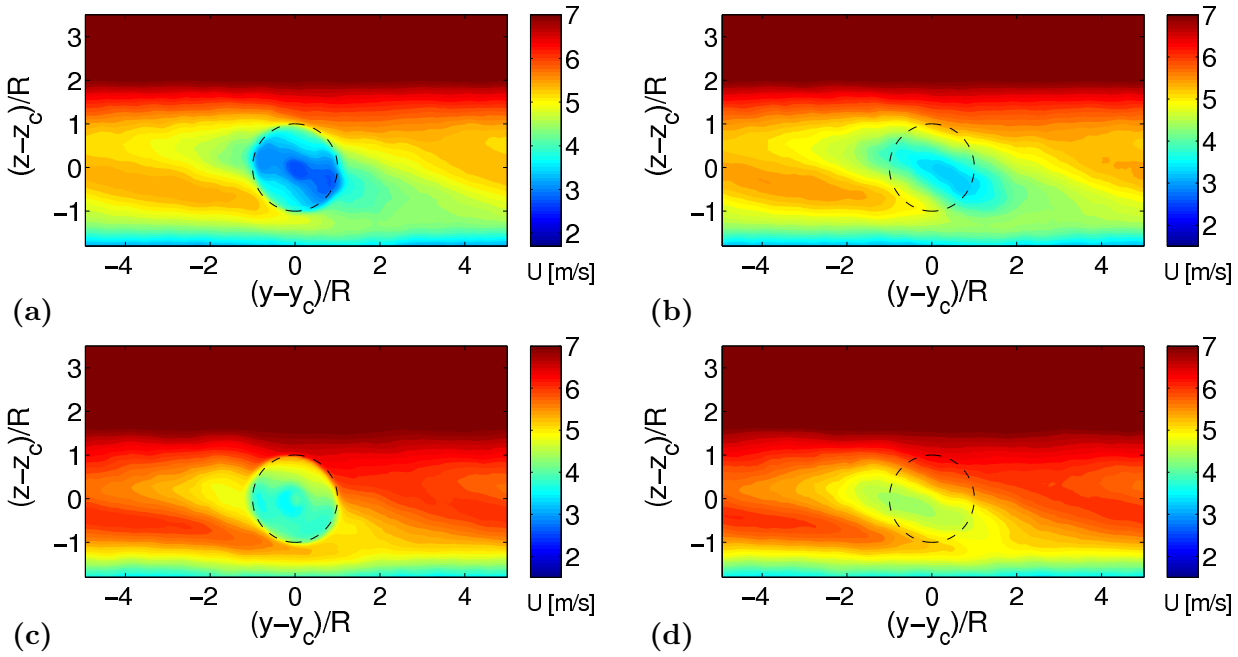

Figure 11: Filled contours of time-averaged (over the last 15 min) x-direction velocity along indicated planes: (a) on the y-z plane downwind 0.5D of the 5D case; (b) on the y-z plane upwind 1D (downwind 4D) of the 5D case; (c) on the y-z plane downwind 0.5D of the 8D case; and (d) on the y-z plane upwind 1D (downwind 7D) of the 8D case. A dashed circle denotes a rotor plane.

wake is skewed strongly. Also, the wake rotation causes the low velocity flow from the bottom of the wake to be transported upwards as the wake travels downwind and expands.

4.4 Wake meandering

Wake meandering is a well-known phenomenon. It is characterized as large scale fluctuation with low frequency. Once the frequency matches a machine's torsional natural vibration frequency, actual damages could occur, such as the failure of the Tacoma Narrows Bridge in 1940 caused by aeroelastic flutter rather than vortex shedding [72].

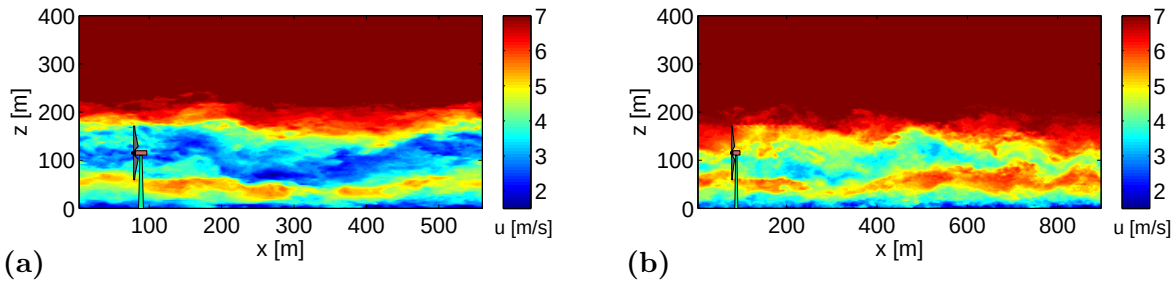

Figure 12: Filled contours of instantaneous x-direction velocity on the x-z plane through the axis of the turbine at the final time: (a) the 5D case; (b) the 8D case.

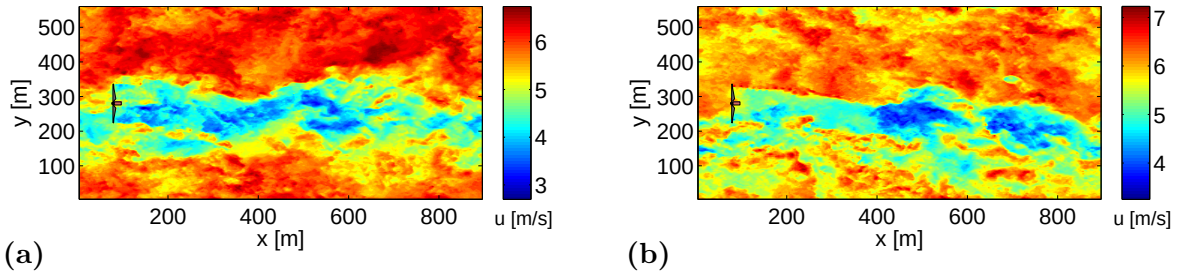

Figure 13: Filled contours of instantaneous x-direction velocity obtained from the 8D case: (a) on the x-y plane at the hub-height $z = z_c$; and (b) on the x-y plane at the height $z = z_c + 0.5R$.

Recently, Medici and Alfredsson [73, 74] performed measurements on a single wind-turbine wake in a wind tunnel. They studied the frequency of wind-turbine wake meandering by using different wind turbines and different set-ups, and identified that this motion is due to an instability of the wake and that it is similar to that of the redlarge-scale coherent structure (so-called von Kármán street) found behind bluff bodies.

Whereas vortex shedding might control the wake-meandering mechanism for high loaded rotors under experimental conditions, Bingöl et al. [75] recently presented redlight-detection-and-ranging (LIDAR) measurements of wake dynamics from a full scale wind turbine located in the field, and results show that the wind-turbine wake is advected passively by the larger-than-rotor-size eddies in the ABL, which is the main contributor to wake meandering in redtheir field study. We support their observation and report that, in the current scenario, the wind-turbine wake meandering is driven by large-scale turbulence in the SBL. Like the gravity waves induced by mountains, islands, etc., the wind-turbine placed in a SBL may induce buoyancy waves. Wind turbines generate not buoyancy waves but, due to kinetic-energy extraction, strong shear layers (an outcome that is clearly manifested in filled contours of instantaneous axial velocity) near wind-turbine edges; moreover, turbulent flows in strong shear layers travel passively with existing buoyancy waves. Figures 12(a), 12(b) and 13(a) show such large-scale fluctuations. The current simulations bear an averaged buoyancy frequency of $N \approx 0.01\,\mathrm{Hz}$ at the wind-turbine height range. Consistent with theories and observations, figure 6 shows that the first mode of the buoyancy waves has already been dominating the large-scale fluctuations, and its resonant modes (such as $2N$) also appear strongly.

Medici and Alfredsson [73, 74] used the non-dimensional Strouhal number, $St = \frac{f \cdot D}{U_\infty}$, to characterize the vortex shedding in wind-turbine wakes, and obtained $St = 0.16$ for large tip-speed ratio three-blade turbines (a typical Strouhal number for bluff-body wakes is 0.2). Based on that, the vortex shedding frequency is approximately 0.006 Hz (assuming the time-space averaged axial velocity in the wind-turbine wake as the velocity scale), which is almost half of the buoyancy frequency. This mode does not appear clearly in figures 6 and 7. Also, as shown in figures 12(a), 12(b) and 13(a), the wavelength of the large-scale fluctuation is approximately 400 m (visual estimation), however, the length scale ($L = U_\infty / f = D/St$) based on the vortex shedding theory is approximately 700m, which is about twice the observed wavelength. Note that in the ABL the length scales of vortex streets generated behind mountains and islands are approximately 5-7 times the length scales of mountains and islands, and are generally 1-2 times larger than the buoyancy wavelengths. Previous field measurements of the Danish Tjæreborg wind farm [76]

reveal that the large-scale fluctuation is characterized by a value of $\frac{f \cdot D}{U_\infty}$ in a range of $0.32 - 0.58$. This is approximately $2 - 3.5$ times the Strouhal number obtained by Medici and Alfredsson [73, 74], and is in better agreement with our present results.

4.5 Coriolis effect

The Ekman spiral refers to a structure of currents or winds near a horizontal boundary in which the flow direction rotates as one moves away from the boundary. The effect is a consequence attributable to the Coriolis force, which causes objects to move to the right of applied forces in the Northern Hemisphere and to the left in the Southern Hemisphere. The laminar solution produces a surface wind parallel to the surface-stress vector and at 45° to the geostrophic wind, a flow angle that is somewhat larger than that observed in real conditions.

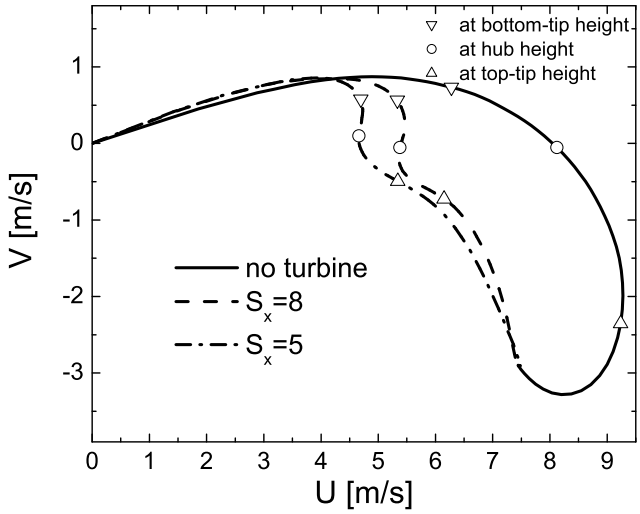

Figure 14: Wind hodographs based on the mean velocities shown in figure 8(a). Solid line: results obtained from the baseline case; dashed line: results obtained from the 8D case; dash dotted line: results obtained from the 5D case; wind-turbine bottom-height, hub-height and tip-height are also illustrated.

The baseline case bears a surface flow angle of approximately 35° (see Fig. 2(b)), which is in good agreement with most real conditions and with the simulation results of many SBL cases including the GABLS case [77, 66, 61, 38]. Figure 14 presents quasi-steady wind hodographs of the baseline case and the two wind-turbine cases. Evidently, the installation of wind-turbines significantly changes the original wind hodograph, including the disappearance of the low-level jet as shown in figure 8(a). It is important to note that, at the wind-turbine top height region, the mean wind direction does not follow the axial direction. In fact, the wind direction rotates clockwise when moving up away from the surface. As shown in figure 13(b), the instantaneous axial-velocity contours of the 8D case at the height of $z = z_c + 0.5R$ clearly manifest the lateral shearing effects. On account of the lateral shear, figure 11 shows a strongly skewed time-averaged axial-velocity distribution in the wake. The rotor diameter chosen in this study is on the same order of the SBL height, thus, the rotor plane covers large areas in which both the axial shear and the lateral shear cannot be avoided. The present results suggest that in the future, developers

of large-sized wind turbines should consider additional loadings on wind turbines coming from lateral shear.

4.6 Turbulence in the wake

A typical design lifetime of modern wind turbines is 20 years. However, many have been dismantled after only a few years of service owing to unsuccessful designs and siting arrangements. The primary cause of failure is that, in a wind farm, the effects of accumulated redwakes can lead to increased fatigue loads on wind turbines. A revision of the standards governing wind turbine design to adequately account for increased fatigue loading in wind-turbine clusters is needed. In this section, we focus on the turbulent velocity fluctuation (which is directly relevant to the fatigue load) in the axial direction since it is dominating compared to the lateral and vertical components as shown by others [2].

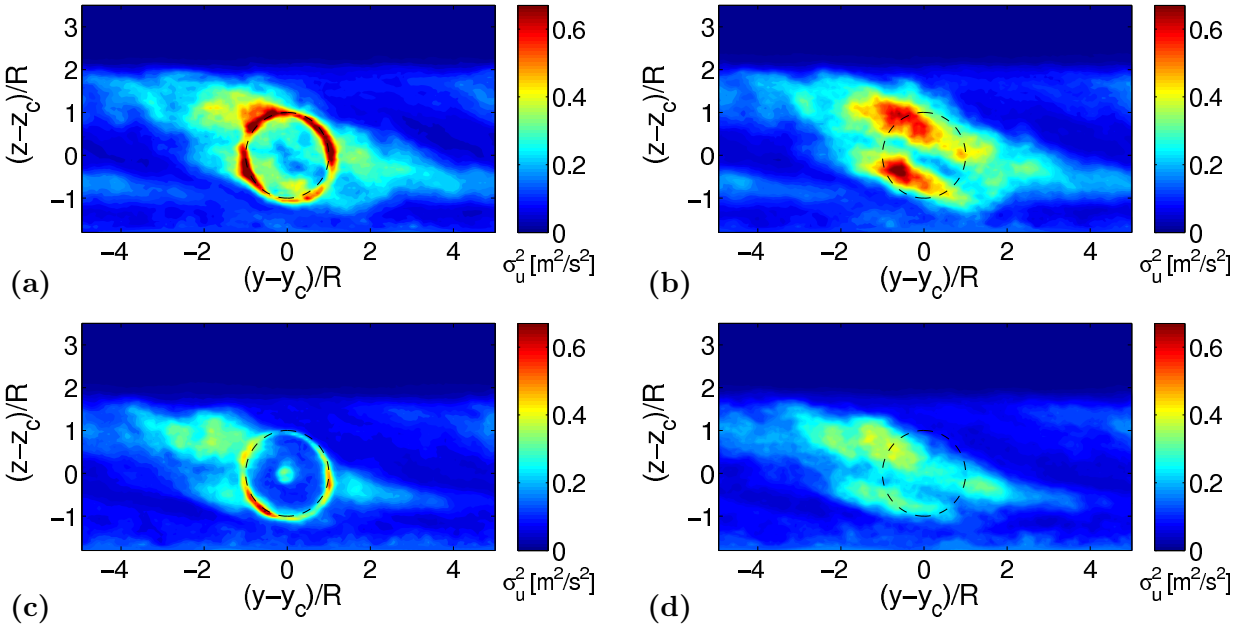

Figure 15: Filled contours of σ_u^2 (measured over the last 15 min) along indicated planes: (a) on the y-z plane downwind 0.5D of the 5D case; (b) on the y-z plane upwind 1D (downwind 4D) of the 5D case; (c) on the y-z plane downwind 0.5D of the 8D case; and (d) on the y-z plane upwind 1D (downwind 7D) of the 8D case. Dashed circle denotes a rotor plane.

Uniform inflow conditions (either laminar or turbulent) were adopted in most prior numerical simulations and wind-tunnel tests. Consequently, these studies yielded axisymmetric distributions of the turbulence levels - the well-known ring-like maxima structure. However, having the wind turbine located in a SBL leads to markedly non-axisymmetric distributions of the turbulence intensity. Figures 15(a) and 15(c) present the filled contours of the axial-velocity variance (local variance of an arbitrary variable is defined as: $\sigma_f^2 = < \widetilde{f}\widetilde{f} >_t - < \widetilde{f} >_t^2$) at 0.5D downwind for the two cases, and figures 15(b) and 15(d) present the filled contours of the axial-velocity variance at 1D upwind. Often regarded as the inflow condition, the turbulence at 1D upwind is of particular importance for wind-turbine safety. As in other single wind-turbine wake studies [2, 55], the ring

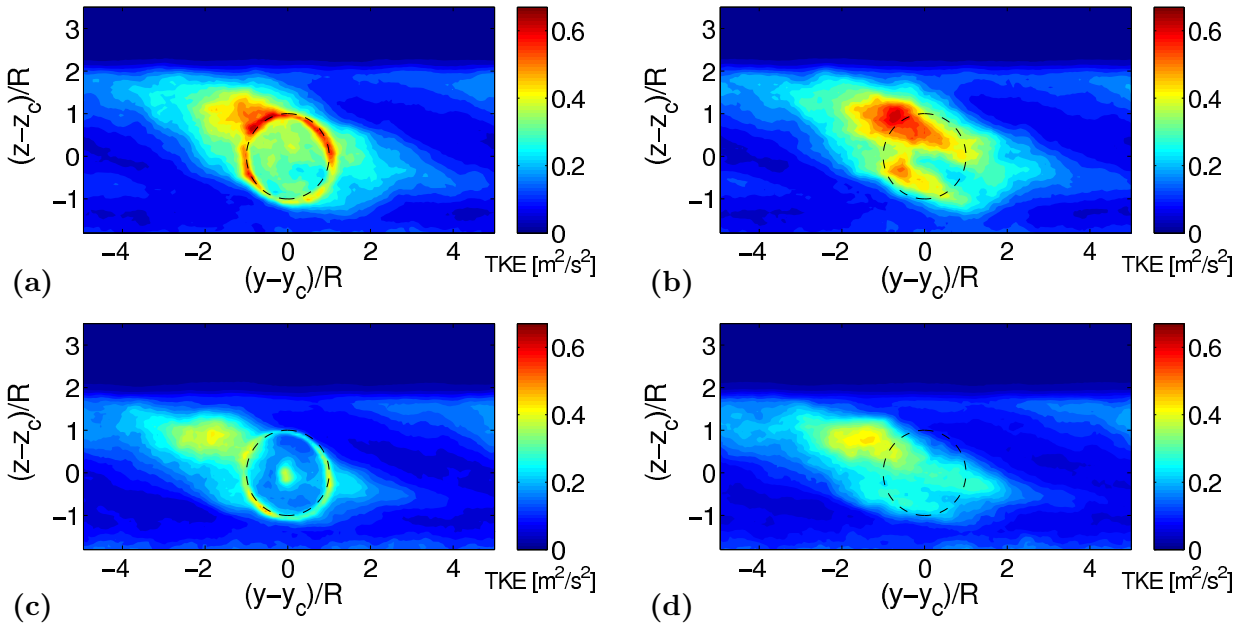

Figure 16: Filled contours of turbulent kinetic energy (measured over the last 15 min) along indicated planes: (a) on the y-z plane downwind 0.5D of the 5D case; (b) on the y-z plane upwind 1D (downwind 4D) of the 5D case; (c) on the y-z plane downwind 0.5D of the 8D case; and (d) on the y-z plane upwind 1D (downwind 7D) of the 8D case. Dashed circle denotes a rotor plane.

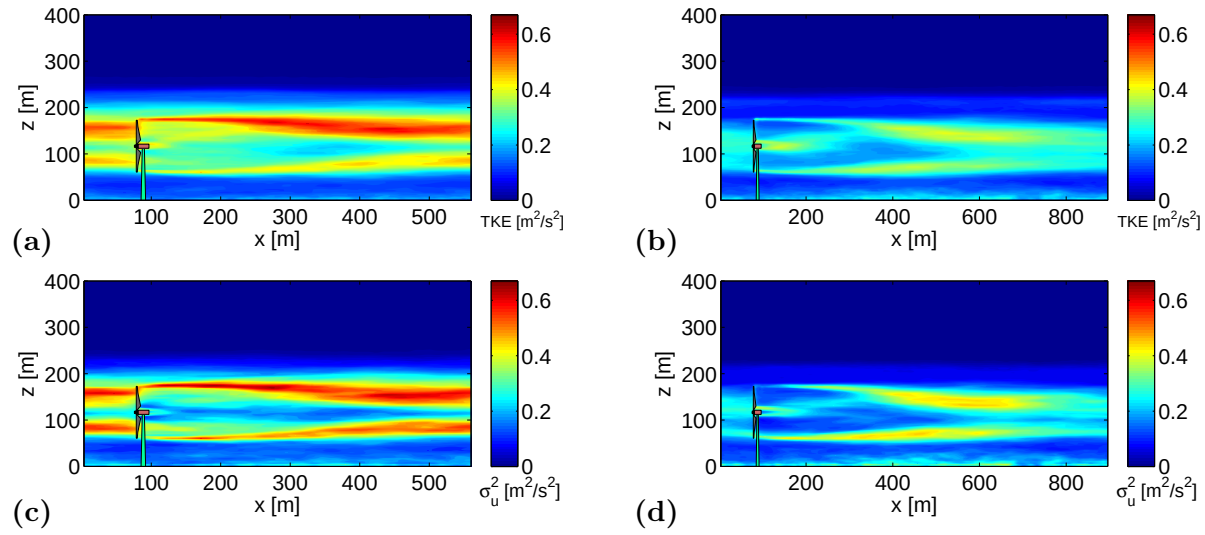

Figure 17: Filled contours of turbulent kinetic energy and σ_u^2 (both measured over the last 15 min) on the x-z plane through the axis of the turbine: TKE obtained from (a) the 5D case; (b) the 8D case; and σ_u^2 obtained from (c) the 5D case; (d) the 8D case.

structure can be observed in the near-wake region (Figs. 15(a) and 15(c)), while it is diffused by the turbulence at longer distances (Figs. 15(b) and 15(d)). In agreement with previous studies of wind-turbine wakes in shear flows, including experiments [70] and simulations [55], the

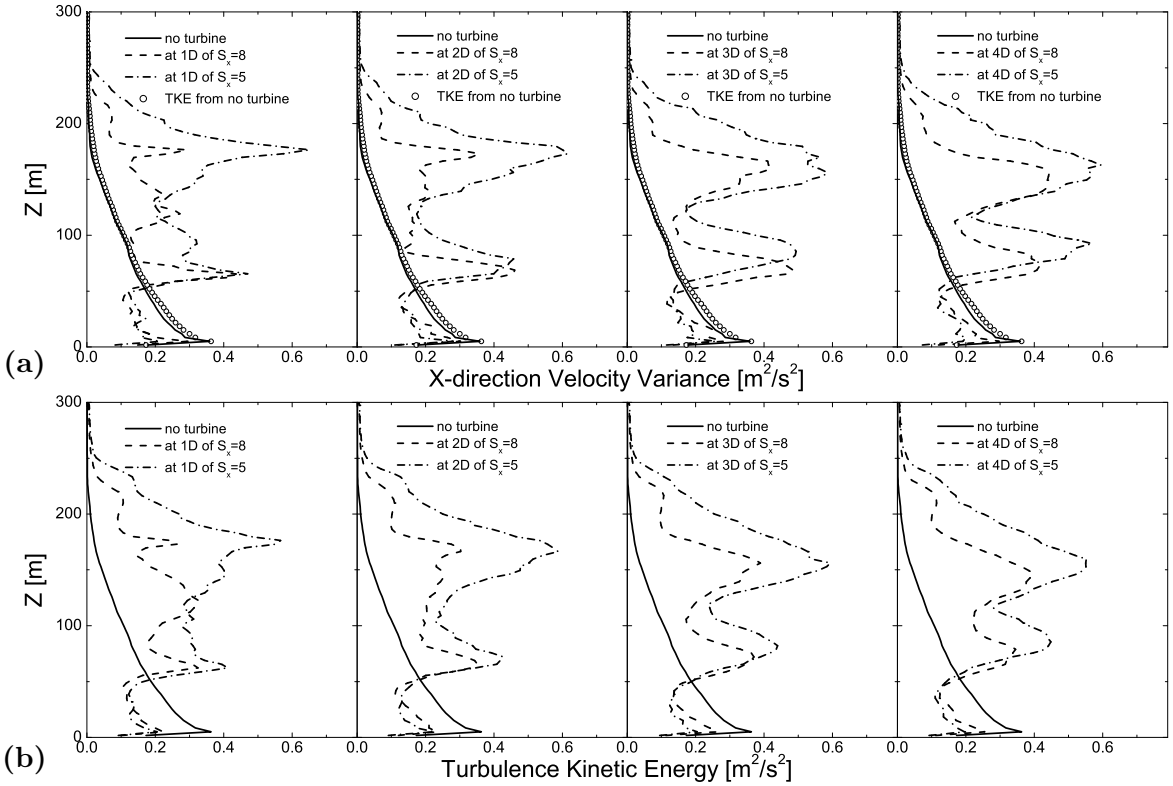

Figure 18: Vertical distribution of (a) σ_u^2 and (b) turbulent kinetic energy (both measured over the last 15 min) obtained from the baseline case (solid), the 8D case (dashed) and the 5D case (dash dotted) through the axis of the turbine at different downwind locations.

turbulence intensity above the hub-height is found to be larger than that below the hub-height. We believe that the primary cause of this is the larger velocity shear (and associated production of turbulence kinetic energy) observed near the turbine top level, as shown in figures 8(a), 9, 12, and 14. Interestingly, the filled contour plots reveal that large amounts of turbulence (by visual estimation, more than approximately 30% as shown in Figs. 15(b) and 15(d)) are transported away from the central wake zone owing to the combined effects of the Coriolis force and the wake rotation. Although the Coriolis force causes lateral shearing, it also leads to a reduction of turbulence levels in the central wake zone, which can reduce the fatigue loads on the wind turbines. In addition, filled contours of the turbulent kinetic energy ($\text{TKE} = \left(\sigma_u^2 + \sigma_v^2 + \sigma_w^2\right)/2$) and the axial-velocity variance on different planes are compared in figures 15, 16 and 17. It is clear that the axial-velocity variance evidently dominates the turbulence structures as mentioned before, thus, the structures of σ_u^2 and TKE are almost identical.

Figure 17 shows filled contours of the axial-velocity variance and the TKE on the x-z plane through the turbine axis. To facilitate a quantitative comparison, figure 18 show vertical profiles of the axial-velocity variance and the TKE for selected downwind locations ($x/D = 1, 2, 3$, and 4). The baseline case results are consistent with other GABLS cases [38]. In the current scenario, turbulence in the wake is notably persistent because each turbine generates turbulence which compensates for the tendency of decay. Further, in agreement with single-turbine experimental

results [70], when wind turbines are placed in the boundary layer, turbulence is reduced below the turbine bottom and significantly enhanced in the wake region. In particular, the maximum levels of turbulence intensity are found at both the top-tip and bottom-tip levels.

Simple models used to estimate turbulence levels inside wind farms often make superposition assumptions to take into account the combined effect of multiple wakes. These codes tend to overestimate turbulence intensities. Confirmed by later studies, Builtjes [78] and Vermeulen and Builtjes [79] found that the turbulence reaches an equilibrium value within wind farms. The time evolution of the turbulence intensity levels inside the simulated wakes (not shown here) supports the statement that there is no outbreak of turbulence intensity in the wind farm and that, instead, the turbulence levels reach a saturation value.

4.7 Turbulent fluxes

In addition to extracting kinetic energy and generating turbulence, wind-turbine blade motions mix fluid parcels. The investigation of fluxes is of interest because local meteorology is considerably affected by the overall exchanges of momentum, heat, moisture, etc. In weather models, the grid-averaged fluxes (averaged over the grid size, typically on the order of several km^2) have to be parameterized. This is typically done using the eddy-viscosity/diffusivity approach, based on the vertical gradients of the mean wind velocity, temperature and moisture concentration.

Figure 19 shows the vertical distributions of mean total (resolved part plus SGS part) vertical flux of axial momentum and heat. The results obtained from the baseline case are consistent with previous GABLS LES studies [61, 38]. Also in agreement with other studies [70], our results show that when wind turbines are immersed in a non-uniform boundary-layer flow that already bears momentum exchanges (negative flux), the magnitude of the negative flux is largest at the top-tip level due to an enhanced vertical mixing of momentum induced by the turbine wakes at that height. This strong mixing and entrainment of relatively warm air (with higher potential virtual temperature) from the free atmosphere, induced by the wind-turbine wakes, leads also to a strong enhancement of the negative heat flux at the top-tip level. It is also important to note that, consistent with the results shown in section 4.1, figures 19(a) and 19(b) also show that the magnitude of the surface momentum and heat fluxes undergo substantial reductions with respect to the no-turbine base case. This reduction is larger than 30% for the surface momentum flux, and larger than 15% for the surface heat flux. Overall, the results presented here indicate that large wind-farms have the potential to impact local meteorology. This conclusion is in agreement with previous low-resolution numerical studies [3].

As mentioned above, large-scale atmospheric models (e.g., weather models) need to parameterize the turbulent fluxes (including the enhanced fluxes produced by the wind farms) as a function of the grid-averaged (at the scale of several km^2) velocity and scalar quantities. This is typically done using simple eddy-diffusion models [80]. One important challenge that one faces when using this approach is the specification of the eddy diffusivity, which is unknown *a-priori*. Here, we compute the vertical profile of the "effective" momentum eddy diffusivity inside the wind farm based on the total momentum fluxes and the mean wind shear obtained with the LES

$$K_m = \frac{\sqrt{\left(<\widetilde{u}'\widetilde{w}'> + <\tau_{xz}>\right)^2 + \left(<\widetilde{v}'\widetilde{w}'> + <\tau_{yz}>\right)^2}}{\sqrt{\left(\frac{\partial <\widetilde{u}>}{\partial z}\right)^2 + \left(\frac{\partial <\widetilde{v}>}{\partial z}\right)^2}} \,. \tag{18}$$

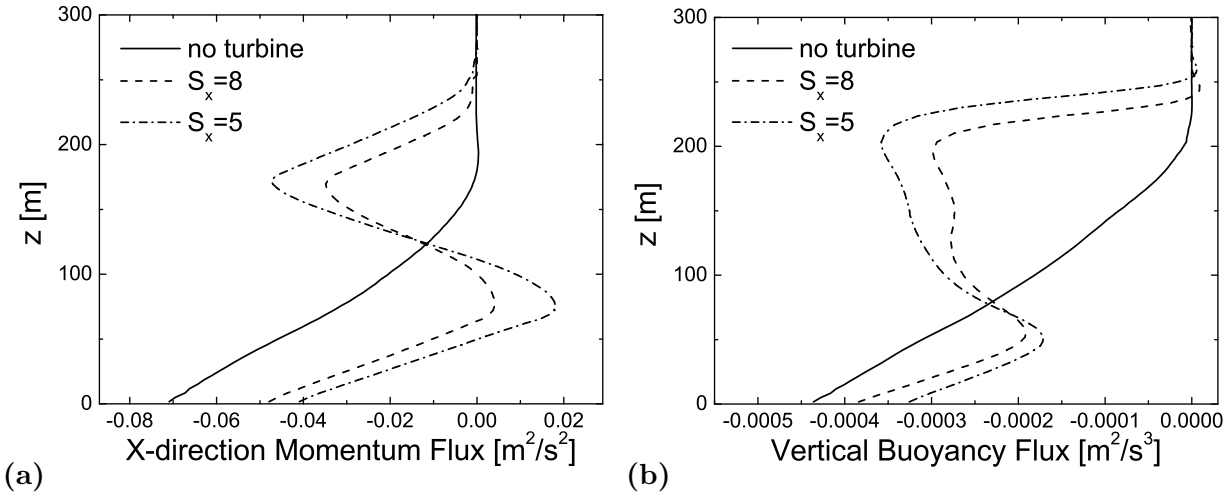

Figure 19: (a) Vertical distribution of axial direction momentum flux; and (b) vertical distribution of buoyancy flux. Solid lines: results obtained from the baseline case; dashed lines: results obtained from the 8D case; dash-dotted lines: results obtained from the 5D case.

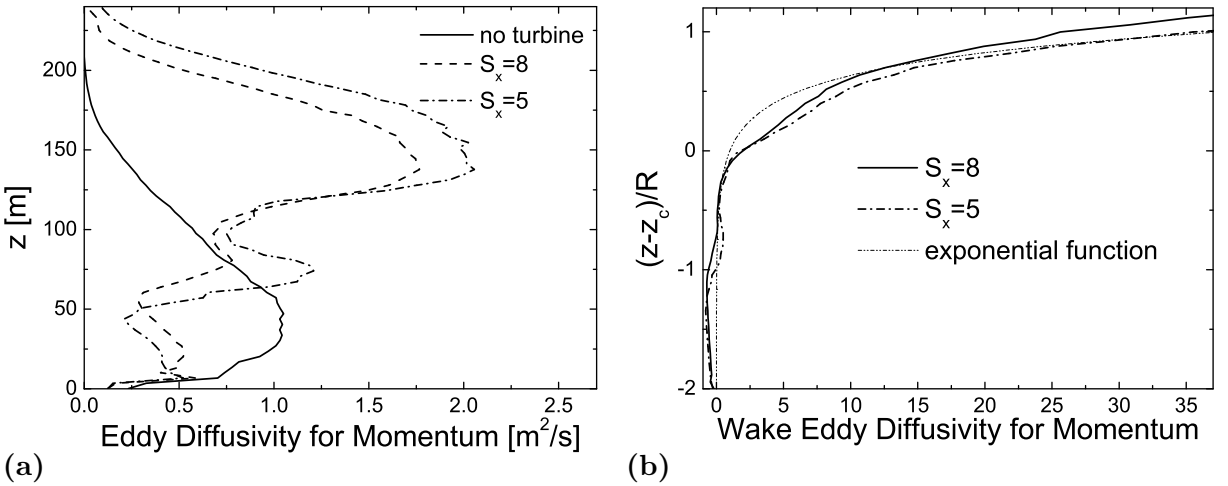

Figure 20: (a) Eddy diffusivity for momentum obtained from the baseline case, the 5D case and the 8D case; (b) wake eddy diffusivity for momentum.

Similarly, the effective heat diffusion is defined as

$$K_h = -\frac{<\widetilde{\theta}'\widetilde{w}'> + <q_3>}{\frac{\partial <\widetilde{\theta}>}{\partial z}} \ . \tag{19}$$

Figures 20(a) and 21(a) show the vertical distributions of eddy diffusivity for momentum and heat obtained from the baseline case and the wind-turbine cases.

The eddy diffusivity profiles obtained from the baseline case are consistent with the ones obtained in GABLS intercomparison studies [61, 80]. Recently, Calaf et al. [19] employed a non-dimensional parameter, called "wake eddy diffusivity," to model the enhancement of wind-turbine mixing. Basically, it is defined as the relative added eddy diffusivity, $K_w = (K_{WT} - K_B)/K_B$,

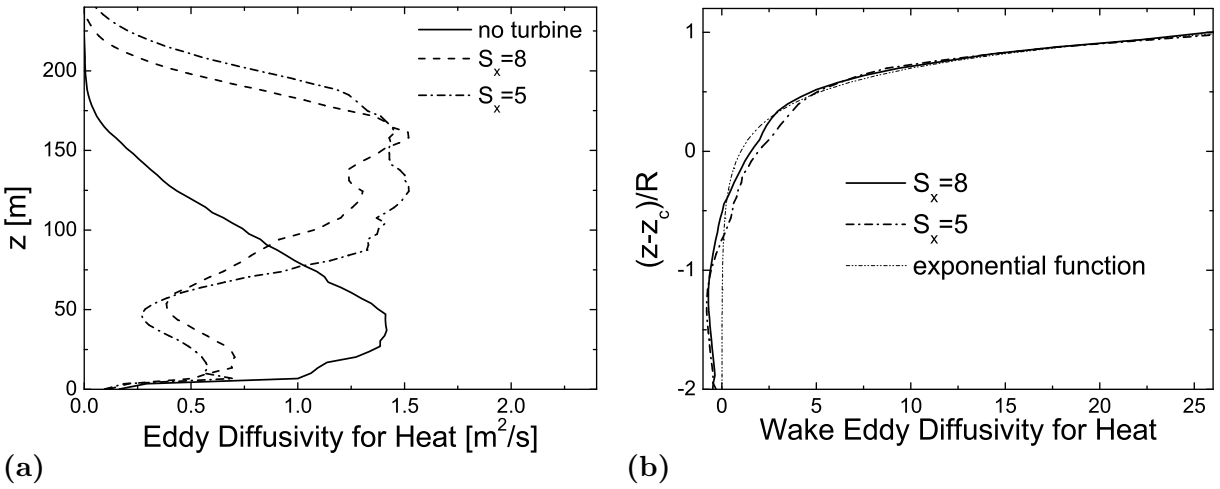

Figure 21: (a) Eddy diffusivity for heat obtained from the baseline case, the 5D case and the 8D case; (b) wake eddy diffusivity for heat.

where the subscript "$_{WT}$" represents the wind-turbine case, and the subscript "$_{B}$" represents the baseline case. Based on relatively low-resolution LES results redobtained using a standard actuator disk model, Calaf et al. [19] introduced reda model for the wake eddy diffusivity for momentum. redIt yields an averaged value (over the range of heights between the top-tip and bottom-tip levels) of 2.4 for the 8D case, and of 3.0 for the 5D case. The wake eddy diffusivities for momentum approximately fit an exponential formulation, $\exp\left(a * (z - z_c)/R\right)$. Integrating over the extent of the rotor yields an averaged (over $(z - z_c)/R = -1{\sim}1$) value of the wake eddy diffusivity of 4.16 ($a = 3.32$) for the 8D case and of 5.19 ($a = 3.63$) for the 5D case. Note that these redvalues are approximately twice the values obtained using redtheir model. redOne possible reason for the discrepancy is the fact that the current simulations are of a wind farm in a relatively shallower stably-stratified boundary layer, which is inherently different from the neutrally-stratified and relatively thicker boundary layer simulated by Calaf et al. [19]. Regarding the eddy diffusivities for heat, the two profiles of the wake eddy diffusivities for heat approximately fit the same exponential formulation given above with $a = 3.30$.

5 Summary and conclusions

The present study reduses a recently developed large-eddy simulation framework [56, 57] to investigate the interactions between a stably-stratified atmospheric boundary layer and a hypothetical very large wind farm. In particular, large-sized wind turbines are "immersed" inside the computational domain of the well-established GABLS LES intercomparison case [61]. This LES framework parameterizes the SGS fluxes of momentum and heat using scale-dependent Lagrangian dynamic models, while the turbine-induced forces are modeled using an actuator line model.

Stable (thermally-stratified) conditions give rise to significant asymmetric loadings owing primarily to high wind shears. Besides the vertical shear associated with the rapid change of wind magnitude with height, there is also considerable horizontal shear due to the change of wind direction with height induced by the Coriolis force. To understand in detail the effects of

wind turbines on the flow structure and the vertical transport of momentum and heat across the boundary layer, the focus of the present study is on instantaneous fields, time-averaged statistics as well as horizontally averaged statistics. Two typical axial spacings, 5D and 8D, have been adopted in this investigation. The results clearly show that discrepancies appear primarily in the distribution of momentum. Specifically, smaller spacing between turbines leads to overall larger extraction of wind power. Also, we found that the 5D case yields noticeably higher boundary layer height and larger turbulence intensity. The differences in the distribution of potential temperature are relatively smaller. An important finding is that the Coriolis force not only causes additional lateral shearing loads on wind turbines, but also drives part of the turbulence energy away from the center of the wind-turbine wakes. These effects should be considered for the prediction of turbulence accumulation in large wind farms under stably-stratified conditions.

Previous studies at relatively low resolutions have shown that wind farms could have noticeable effects on the global climate [4, 6], and on local meteorology [3]. In agreement with these studies, present results show that the wind-turbine motions enhance the vertical mixing of heat, resulting in increased air temperatures in the wind-turbine wakes and lowered surface heat flux, thus affecting the thermal energy budget. The wind in the lowest part of the atmosphere is the most important atmospheric variable for wind-power meteorology. A detailed understanding of the wind-turbine wakes can be useful in providing more accurate parameterizations of turbulent fluxes in weather/climate simulations. In the last decade, researchers have introduced an effective roughness approach [81, 19] and some [82] have used it to parameterize the effects of wind-turbine arrays. However, two issues should be noticed: (i) with the growth of computational power as well as the rapid increase in wind-turbine sizes, numerical studies have become capable of resolving the layers below the wind-turbine bottom-tip level [4]; accordingly, this approach is increasingly inaccurate in simulating surface layers, and may induce large errors because it is not able to account for the strong flow inhomogeneity as well as anisotropy in the near-wall region; (ii) the usage of the effective roughness is based on the similarity theory [83, 64], which is technically applicable to the surface layer (the lowest $10\% - 20\%$ of the flow in the ABL); nowadays the top-tip level of redlarge-sized wind turbines may extend to a height on the same order as the boundary-layer height, especially during nighttime; therefore, in many situations, representing the wind turbines with an effective roughness parameter becomes impractical.

The results presented here indicate that large-eddy simulation can provide valuable three-dimensional high-resolution velocity and temperature fields needed for the quantitative description of wind-turbine wakes, and their effects on the turbulent fluxes of heat and momentum inside and above wind farms. Although previous validation of the LES framework has been performed using experimental measurements [56, 57] and field measurements [57], it still bears some issues in its present constitution: (i) the actuator line method is sensitive to the quality of airfoil data; and (ii) simulations should encompass more realistic physics and a variety of atmospheric conditions. These include the breakdown of the periodic boundary conditions in horizontal directions, and the consideration of other inflow and surface boundary conditions, wind-farm configurations, and the effects of topography, air moisture, and the like. Future studies will use the LES framework to further study the effects of wind-farm size, atmospheric stability (neutral, convective and stable), topography, and wind-farm configuration. Furthermore, wind-tunnel experiments (using particle image velocimetry and hot/cold-wire anemometry) and field studies red(using sonic detection and ranging (SODAR) devices, LIDARs, etc.) can provide additional insights as well as validation data sets for the LES framework. Also, there is a need for reliable coupling of LES with weather

models to account for the effects of large-scale atmospheric forcing.

6 Acknowledgments

This research was supported by the Swiss National Science Foundation (grant 200021_132122), the National Science Foundation (grant ATM-0854766), NASA (grant NNG06GE256), customers of Xcel Energy through a grant (RD3-42) from the Renewable Development Fund, and the University of Minnesota Institute for Renewable Energy and the Environment. Computing resources were provided by the Minnesota Supercomputing Institute.

References

[1] E. L. Petersen, N. G. Mortensen, L. Landberg, J. Højstrup, and H. P. Frank, "Wind power meteorology. part I: Climate and turbulence," *Wind Energy*, vol. 1, pp. 25–45, 1998.

[2] L. J. Vermeer, J. N. Sørensen, and A. Crespo, "Wind turbine wake aerodynamics," *Progress Aero. Sci.*, vol. 39, pp. 467–510, 2003.

[3] S. Baidya Roy, S. W. Pacala, and R. L. Walko, "Can large wind farms affect local meteorology?," *J. Geophys. Res.*, vol. 109, pp. 1–6, 2004.

[4] D. W. Keith, J. F. DeCarolis, D. C. Denkenberger, D. H. Lenschow, S. L. Malyshev, S. Pacala, and P. J. Rasch, "The influence of large-scale wind power on global climate," *PNAS*, vol. 101, Nov. 2004.

[5] M. O. L. Hansen, J. N. Sørensen, S. Voutsinas, N. Sørensen, and H. A. Madsen, "State of the art in wind turbine aerodynamics and aeroelasticity," *Progress Aero. Sci.*, vol. 42, pp. 285–330, 2006.

[6] D. B. Kirk-Davidoff and D. W. Keith, "On the climate impact of surface roughness anomalies," *J. Atmos. Sci.*, vol. 65, pp. 2215–2234, 2008.

[7] G. Xu and L. N. Sankar, "Computational study of horizontal axis wind turbines," *J. Sol. Energy Eng.*, vol. 122, no. 1, pp. 35–39, 2000.

[8] C. Alinot and C. Masson, "Aerodynamic simulations of wind turbines operating in atmospheric boundary layer with various thermal stratifications," *ASME Wind Energy Symposium*, vol. AIAA, pp. 2002–42, 2002.

[9] N. N. Sørensen, J. A. Michelsen, and S. Schreck, "Navier-stokes predictions of the NREL phase VI rotor in the NASA Ames 80ft * 120ft wind tunnel," *Wind Energy*, vol. 5, pp. 151–169, 2002.

[10] R. Gómez-Elvira, A. Crespo, E. Migoya, and J. Manuel F. Hernández, "Anisotropy of turbulence in wind turbine wakes," *J. Wind. Eng. Ind. Aerodyn.*, vol. 93, pp. 797–814, 2005.

[11] C. Tongchitpakdee, S. Benjanirat, and L. N. Sankar, "Numerical simulation of the aerodynamics of horizontal axis wind turbines under yawed flow conditions," *J. Sol. Energy Eng.*, vol. 127, no. 4, pp. 464–474, 2005.

[12] N. Sezer-Uzol and L. N. Long, "3-D time-accurate CFD simulations of wind turbine rotor flow fields," *AIAA Paper 2006-0394*, 2006.

[13] A. E. Kasmi and C. Masson, "An extended $\kappa-\varepsilon$ model for turbulent flow through horizontal-axis wind turbines," *J. Wind. Eng. Ind. Aerodyn.*, vol. 96, pp. 103–122, 2008.

[14] AGARD, "A selection of test cases for the validation of large-eddy simulations of turbulent flows," *AGARD Advisory Report*, vol. 345, 1998.

[15] S. B. Pope, *Turbulent flows*. Cambridge University Press, Cambridge, 2000.

[16] P. Sagaut, *Large eddy simulation for incompressible flows*. Springer-Verlag, Berlin Heidelberg, 3rd ed., 2006.

[17] A. Jimenez, A. Crespo, E. Migoya, and J. Garcia, "Advances in large-eddy simulation of a wind turbine wake," *J. Phys.: Conf. Ser.*, vol. 75, p. 012041, 2007.

[18] A. Jimenez, A. Crespo, E. Migoya, and J. Garcia, "Large-eddy simulation of spectral coherence in a wind turbine wake," *Environ. Res. Lett.*, vol. 3, p. 015004, 2008.

[19] M. Calaf, C. Meneveau, and J. Meyers, "Large eddy simulation study of fully developed wind-turbine array boundary layers," *Phys. Fluids*, vol. 22, 2010.

[20] J. W. Deardorff, "The use of subgrid transport equations in a three-dimensional model of atmospheric turbulence," *J. Fluids Eng.*, vol. 95, pp. 429–438, 1973.

[21] P. J. Mason and S. H. Derbyshire, "Large-eddy simulation of the stably-stratified atmospheric boundary layer," *Boundary-Layer Meteorol.*, vol. 53, pp. 117–162, October 1990.

[22] C. Meneveau and T. S. Lund, "The dynamic Smagorinsky model and scale-dependent coefficients in the viscous range of turbulence," *Phys. Fluids*, vol. 9, pp. 3932–3934, December 1997.

[23] F. Porté-Agel, M. Pahlow, C. Meneveau, and M. B. Parlange, "Atmospheric stability effect on subgrid-scale physics for large-eddy simulation," *Adv. Water Resour.*, vol. 24, pp. 1085–1102, 2001.

[24] F. Porté-Agel, C. Meneveau, and M. B. Parlange, "A scale-dependent dynamic model for large-eddy simulation: application to a neutral atmospheric boundary layer," *J. Fluid Mech.*, vol. 415, pp. 261–284, 2000.

[25] R. Stoll and F. Porté-Agel, "Dynamic subgrid-scale models for momentum and scalar fluxes in large-eddy simulations of neutrally stratified atmospheric boundary layers over heterogeneous terrain," *Water. Resour. Res.*, vol. 42, p. W01409, 2006.

[26] R. Stoll and F. Porté-Agel, "Large-eddy simulation of the stable atmospheric boundary layer using dynamic models with different averaging schemes," *Boundary-Layer Meteorol.*, vol. 126, pp. 1–28, July 2008.

[27] F. Wan, F. Porté-Agel, and R. Stoll, "Evaluation of dynamic subgrid-scale models in large-eddy simulations of neutral turbulent flow over a two-dimensional sinusoidal hill," *Atmos. Env.*, vol. 41, no. 13, pp. 2719–2728, 2007.

[28] F. Wan and F. Porté-Agel, "Large-eddy simulation of stably-stratified flow over a steep hill," *Boundary-Layer Meteorol.*, vol. 138, no. 3, pp. 367–384, 2011.

[29] R. E. Froude, "On the part played in propulsion by difference of fluid pressure," *Trans. Roy. Inst. Naval Arch.*, vol. 30, pp. 390–423, 1889.

[30] W. J. M. Rankine, "On the mechanical principles of the action of propellers," *Trans. Roy. Inst. Naval Arch.*, vol. 6, pp. 13–39, 1865.

[31] H. Glauert, *Aerodynamic theory*, ch. "Airplane propellers", pp. 169–360. edited by W. F. Durand (Dover, New York), 1963.

[32] J. N. Sørensen and W. Z. Shen, "Numerical modeling of wind turbine wakes," *J. Fluids Eng.*, vol. 124, pp. 393–399, 2002.

[33] N. Troldborg, J. N. Sørensen, and R. Mikkelsen, "Actuator line simulation of wake of wind turbine operating in turbulent inflow," *J. of Phys.: Conf. Series*, vol. 75, July 2007.

[34] S. Ivanell, J. N. Sørensen, R. Mikkelsen, and D. Henningson, "Analysis of numerically generated wake structures," *Wind Energy*, vol. 12, pp. 63–80, 2009.

[35] J. D. Albertson and M. B. Parlange, "Natural integration of scalar fluxes from complex terrain," *Advan. Water Resour.*, vol. 23, pp. 239–252, 1999.

[36] F. Porté-Agel, "A scale-dependent dynamic model for scalar transport in large-eddy simulations of the atmospheric boundary layer," *Boundary-Layer Meteorol.*, vol. 112, no. 1, pp. 81–105, 2004.

[37] R. Stoll and F. Porté-Agel, "Effect of roughness on surface boundary conditions for large-eddy simulation," *Boundary-Layer Meteorol.*, vol. 118, pp. 169–187, January 2006.

[38] S. Basu and F. Porté-Agel, "Large-eddy simulation of stably stratified atmospheric boundary layer turbulence: A scale-dependent dynamic modeling approach," *J. Atmos. Sci.*, vol. 63, pp. 2074–2091, 2006.

[39] H. Lu and F. Porté-Agel, "A modulated gradient model for large-eddy simulation: application to a neutral atmospheric boundary layer," *Phys. Fluids*, vol. 22, p. 015109, 2010.

[40] J. Smagorinsky, "General circulation experiments with the primitive equations: I. the basic experiment," *Mon. Weather Rev.*, vol. 91, no. 3, pp. 99–164, 1963.

[41] D. K. Lilly, "The representation of small-scale turbulence in numerical simulation experiments," *Proc. IBM Sci. Com. Symp. Environmental Sciences (Yorktown Heights, N.Y.)*, p. 167, 1967.

[42] M. Antonopoulos-Domis, "Large-eddy simulation of a passive scalar in isotropic turbulence," *J. Fluid Mech.*, vol. 104, pp. 55–79, 1981.

[43] J. Kleissl, C. Meneveau, and M. B. Parlange, "On the magnitude and variability of subgrid-scale eddy-diffusion coefficients in the atmospheric surface layer," *J. Atmos. Sci.*, vol. 60, pp. 2372–2388, 2003.

[44] J. Kleissl, M. B. Parlange, and C. Meneveau, "Field experimental study of dynamic smagorinsky models in the atmospheric surface layer," *J. Atmos. Sci.*, vol. 61, pp. 2296–2307, 2004.

[45] E. Bou-Zeid, N. Vercauteren, M. B. Parlange, and C. Meneveau, "Scale dependence of subgrid-scale model coefficients: an a priori study," *Phys. Fluids*, vol. 20, 2008.

[46] P. J. Mason and D. J. Thomson, "Stochastic backscatter in large-eddy simulations of boundary layers," *J. Fluid Mech.*, vol. 242, pp. 51–78, 1992.

[47] P. J. Mason, "Large-eddy simulation: a critical review of the technique," *Q. J. R. Meteorol. Soc.*, vol. 120, pp. 1–26, 1994.

[48] P. J. Mason and A. R. Brown, "On subgrid models and filter operations in large eddy simulations," *J. Atmos. Sci.*, vol. 56, pp. 2101–2114, 1999.

[49] M. Germano, U. Piomelli, and W. H. Cabot, "A dynamic subgrid-scale eddy viscosity model," *Phys. Fluids A*, vol. 3, pp. 1760–1765, July 1991.

[50] P. Moin, K. D. Squires, and S. Lee, "A dynamic subgrid-scale model for compressible turbulence and scalar transport," *Phys. Fluids*, vol. 3, pp. 2746–2757, 1991.

[51] F. Porté-Agel, C. Meneveau, M. B. Parlange, and W. E. Eichinger, "A priori field study of the subgrid-scale heat fluxes and dissipation in the atmospheric surface layer," *J. Atmos. Sci.*, vol. 58, pp. 2673–2698, 2001.

[52] D. K. Lilly, "A proposed modification of the Germano subgrid-scale closure method," *Phys. Fluids*, vol. 4, pp. 633–635, March 1992.

[53] C. Meneveau, T. S. Lund, and W. H. Cabot, "A lagrangian dynamic subgrid-scale model of turbulence," *J. Fluid Mech.*, vol. 319, pp. 353– 385, 1996.

[54] S. Mathew, *Wind energy: fundamentals, resource analysis and economics*. Springer-Verlag, Berlin Heidelberg, 2006.

[55] N. Troldborg, *Actuator Line Modeling of Wind Turbine Wakes*. PhD thesis, Dept. of Mechanical Engineering, Technical Univ. of Denmark, 2008.

[56] Y.-T. Wu and F. Porté-Agel, "LES of wind-turbine wakes: Evaluation of turbine parameterizations," *Boundary-Layer Meteorol.*, vol. 138, no. 3, pp. 345–366, 2011.

[57] F. Porté-Agel, Y.-T. Wu, H. Lu, and R. Conzemius, "Large-eddy simulation of atmospheric boundary layer flow through wind turbines and wind farms," *J. Wind Eng. Ind. Aerodyn.*, vol. 99, no. 4, pp. 154–168, 2011.

[58] T. Burton, D. Sharpe, N. Jenkins, and E. Bossanyi, *Wind energy handbook*. John Wiley & Sons, Ltd, Baffins Lane, Chichester, England, 2001.

[59] J. F. Manwell, J. G. McGowan, and A. L. Rogers, *Wind Energy Explained: Theory, Design and Application*. John Wiley & Sons, Ltd, Baffins Lane, Chichester, England, 2002.

[60] W. Z. Shen, M. O. L. Hansen, and J. N. Sørensen, "Determination of the angle of attack on rotor blades," *Wind Energy*, vol. 12, pp. 91–98, 2009.

[61] R. J. Beare, M. K. Macvean, A. A. M. Holtslag, J. Cuxart, I. Esau, J.-C. Golaz, M. A. Jimenez, M. Khairoutdinov, B. Kosovic, D. Lewellen, T. S. Lund, J. K. Lundquist, A. Mccabe, A. F. Moene, Y. Noh, S. Raasch, and P. Sullivan, "An intercomparison of large-eddy simulations of the stable boundary layer," *Boundary-Layer Meteorol.*, vol. 118, no. 2, pp. 247–272, 2006.

[62] P. Fuglsang and C. Bak, "Development of the Risø wind turbine airfoil," *Wind Energy*, vol. 7, pp. 145–162, 2004.

[63] C. Canuto, M. Y. Hussaini, A. Quarteroni, and T. A. Zang, *Spectral methods in fluid dynamics*. Sprnger-Verlag, Berlin Heidelberg, 1988.

[64] J. A. Businger, J. C. Wynagaard, Y. Izumi, and E. F. Bradley, "Flux-profile relationships in the atmospheric surface layer," *J. Atmos. Sci.*, vol. 28, pp. 181–189, 1971.

[65] R. J. Beare and M. K. Macvean, "Resolution sensitivity and scaling of large-eddy simulations of the stable boundary layer," *Boundary-Layer Meteorol.*, vol. 112, no. 2, pp. 257–281, 2004.

[66] B. Kosovic and J. A. Curry, "A large eddy simulation study of a quasi-steady, stably strati ed atmospheric boundary layer," *J. Atmos. Sci.*, vol. 57, pp. 1052–1068, April 2000.

[67] See supplementary material at (link) for flow visualization with iso-surface of vorticity (revealing helicoidal tip vortices) and filled contours of instantaneous x-direction velocity on the vertical plane through the axis of the turbine revealing tip vortices.

[68] J. Jeong and F. Hussain, "On the identification of a vortex," *J. Fluid Mech.*, vol. 285, pp. 69–94, 1995.

[69] F. Massouh and I. Dobrev, "Exploration of the vortex wake behind of wind turbine rotor," *J. of Phys.: Conf. Series*, vol. 75, July 2007.

[70] L. P. Chamorro and F. Porté-Agel, "A wind-tunnel investigation of wind-turbine wakes: Boundary-layer turbulence effects," *Boundary-Layer Meteorol.*, vol. 132, pp. 129–149, April 2009.

[71] F. Zahle, N. N. Sørensen, and H. A. Madsen, *Research in aeroelasticity EFP-2007*, ch. "The influence of wind shear and tower presence on rotor and wake aerodynamics using CFD", pp. 17–34. edited by C. Bak (Risø National Laboratory, Technical University of Denmark, Roskilde, Denmark), 2008.

[72] K. Y. Billah and R. H. Scanlan, "Resonance, tacoma narrows bridge failure, and undergraduate physics textbooks," *Am. J. Phys.*, vol. 59, no. 2, pp. 118–124, 1991.

[73] D. Medici and P. H. Alfredsson, "Measurements on a wind turbine wake: 3D effects and bluff body vortex shedding," *Wind Energy*, vol. 9, pp. 219–236, 2006.

[74] D. Medici and P. H. Alfredsson, "Measurements behind model wind turbines: Further evidence of wake meandering," *Wind Energy*, vol. 11, pp. 211–217, 2008.

[75] F. Bingöl, J. Mann, and G. C. Larsen, "Light detection and ranging measurements of wake dynamics Part I: One-dimensional scanning," *Wind Energy*, vol. 13, pp. 51–61, 2010.

[76] G. C. Larsen, H. A. Madsen, T. J. Larsen, and N. Troldborg, "Wake modeling and simulation," *Risø-R-1653(EN), Risø-R-Report*, 2008.

[77] G. N. Coleman, J. H. Ferziger, and P. R. Spalart, "Direct simulation of the stably stratified turbulent Ekman layer," *J. Fluid Mech.*, vol. 244, pp. 677–712, 1992.

[78] P. J. H. Builtjes, "The interaction of windmill wakes," *Proceedings of the 2nd International Symposium on Wind Energy Systems, BHRA Fluid Engineering, Amsterdam, Netherlands*, pp. B5–49–58, 1978.

[79] P. E. J. Vermeulen and P. J. H. Builtjes, "Turbulence measurements in simulated wind turbine clusters," *Report 82-03003, TNO Division of Technology for Society*, 1982.

[80] J. Cuxart, A. A. M. Holtslag, R. J. Beare, E. Bazile, A. Beljaars, A. Cheng, L. Conangla, M. Ek, F. Freedman, R. Hamdi, A. Kerstein, H. Kitagawa, G. Lenderink, D. Lewellen, J. Mailhot, T. Mauritsen, V. Perov, G. Schayes, G.-J. Steeneveld, G. Svensson, P. Taylor, W. Weng, S. Wunsch, and K.-M. Xu, "Single-column model intercomparison for a stably stratified atmospheric boundary layer," *Boundary-Layer Meteorol.*, vol. 118, no. 2, pp. 273–303, 2006.

[81] S. Frandsen, R. Barthelmie, S. Pryor, O. Rathmann, S. Larsen, J. Hojstrup, and M. Thogersen, "Analytical modelling of wind speed de cit in large offshore wind farms," *Wind Energy*, vol. 9, pp. 39–53, 2006.

[82] D. B. Barrie and D. B. Kirk-Davidoff, "Weather response to management of a large wind turbine array," *Atmos. Chem. Phys. Discuss.*, vol. 9, pp. 2917–2931, 2009.

[83] T. von Kármán, "Mechanical similitude and turbulence," *Tech. Mem., No. 611, Washington D.C., NACA*, 1931.